Contributions of mirror-image hair cell orientation to mouse otolith organ and zebrafish neuromast function

Kazuya Ono[#1], Amandine Jarysta[#2], Natasha Hughes[#3], Alma Jukic[#4], Vanessa Chang[3], Michael R. Deans[5,6], Ruth Anne Eatock*[1], Kathleen Cullen*[3,7,8,9], Katie Kindt*[4] and Basile Tarchini[*2,10]

[1] Department of Neurobiology, University of Chicago, Chicago, IL, 60637, USA.
[2] The Jackson Laboratory, Bar Harbor, ME 04609, USA.
[3] Dept. of Biomedical Engineering, Johns Hopkins University, Baltimore, 21205 MD, USA
[4] Section on Sensory Cell Development and Function, National Institute on Deafness and Other Communication Disorders, National Institutes of Health, Bethesda, MA, USA
[5] Department of Neurobiology, Spencer Fox Eccles School of Medicine, University of Utah, Salt Lake City, Utah, USA.
[6] Department of Otolaryngology - Head & Neck Surgery, Spencer Fox Eccles School of Medicine at the University of Utah, Salt Lake City, Utah, USA.
[7] Department of Otolaryngology-Head and Neck Surgery, Johns Hopkins University, Baltimore 21205 MD, USA.
[8] Department of Neuroscience, Johns Hopkins University, Baltimore 21205 MD, USA.
[9] Kavli Neuroscience Discovery Institute, Johns Hopkins University, Baltimore 21205 MD, USA.
[10] Tufts University School of Medicine, Boston, MA 02111, USA.

[#] co-first authors
[*] Corresponding authors

SUMMARY/ABSTRACT

Otolith organs in the inner ear and neuromasts in the fish lateral-line harbor two populations of hair cells oriented to detect stimuli in opposing directions. The underlying mechanism is highly conserved: the transcription factor EMX2 is regionally expressed in just one hair cell population and acts through the receptor GPR156 to reverse cell orientation relative to the other population. In mouse and zebrafish, loss of Emx2 results in sensory organs that harbor only one hair cell orientation and are not innervated properly. In zebrafish, Emx2 also confers hair cells with reduced mechanosensory properties. Here, we leverage mouse and zebrafish models lacking GPR156 to determine how detecting stimuli of opposing directions serves vestibular function, and whether GPR156 has other roles besides orienting hair cells. We find that otolith organs in *Gpr156* mouse mutants have normal zonal organization and normal type I-II hair cell distribution and mechano-electrical transduction properties. In contrast, *gpr156* zebrafish mutants lack the smaller mechanically-evoked signals that characterize Emx2-positive hair cells. Loss of GPR156 does not affect orientation-selectivity of afferents in mouse utricle or zebrafish neuromasts. Consistent with normal otolith organ anatomy and afferent selectivity, *Gpr156* mutant mice do not show overt vestibular dysfunction. Instead, performance on two tests that engage otolith organs is significantly altered – swimming and off-vertical-axis rotation. We conclude that GPR156 relays hair cell orientation and transduction information downstream of EMX2, but not selectivity for direction-specific afferents. These results clarify how molecular mechanisms that confer bi-directionality to sensory organs contribute to function, from single hair cell physiology to animal behavior.

INTRODUCTION

The vestibular system provides essential information about the head's motion and orientation relative to gravity and plays a vital role in everyday life. Fundamental gaps exist in our understanding of vestibular development and function. For example, we do not fully understand how the abrupt reversal of hair cell (HC) orientation in otolith organs affects vestibular function, and whether the reversal also impacts HC mechano-electrical transduction properties or afferent neuron contacts. We explore these questions further in mouse and in the zebrafish lateral line, a sensory system where external fluid flow is detected by neuromast organs that also feature HC reversal.

Vestibular HCs reside in five sensory organs per inner ear in human, mouse and larval zebrafish: three cristae ampullaris and two otolith (or macular) organs. Within each of these organs, HCs are precisely oriented to detect mechanical stimuli based on direction. HCs are sensitive to the proportion of a stimulus aligned with the mechanosensory hair bundle's orientation: a vector from the bundle's short edge to its tall (kinociliary) edge. In cristae, which detect angular head motions, HCs are oriented uniformly to detect fluid flow in the plane of the attached semicircular canal. In contrast, HCs in otolith organs are oriented to respond to a range of head positions and linear motions in an approximately horizontal (utricle) or vertical (saccule) plane (Fig. 1A). Within these planes, HCs show two opposing orientations across a virtual "line of polarity reversal" (LPR), a conserved anatomical feature in all otolith organs (Denman-Johnson and Forge, 1999; Flock, 1964; Lindeman, 1969). HCs are also aligned in two opposing orientations in fish and amphibian neuromasts in the lateral-line system. Orientation reversal confers on neighboring HCs of opposing orientations opposite responses to the same local stimulus: depolarization and increased afferent spike rate in one population, but hyperpolarization and decreased spike rate in the other. This functional prediction and its utility are well established in neuromasts as the ability to sensitively detect water movements in two directions (Chitnis et al., 2012; Lopez-Schier et al., 2004). Beyond increasing the range of stimulus orientations detected, it remains unclear how HCs with opposing orientations and responses serve otolith organ function.

In the utricle, the LPR also segregates distinct zones, for example the lateral extrastriola (LES) from the more medial striola (Fig. 1A). Zones are strikingly different regions found in all vestibular epithelia, with ‘central’ and ‘peripheral’ zones of cristae corresponding to striolar and extrastriolar zones of maculae, respectively. Afferents that innervate striolar HCs have irregular spike timing and adapting responses in contrast to afferents that innervate extrastriolar HCs which have more regular and tonic spikes (Goldberg, 1991; Goldberg, 2000). Striolar afferents transmit more information about the time course of translational self-motion, while extrastriolar afferents better discriminate between different static head orientations relative to gravity (Jamali et al., 2019). Correlated with these physiological differences between zones are differences in HCs and afferent morphologies. Both the striola and extrastriola are populated by type I HCs contacted by *calyx afferent endings* and type II HCs contacted by *bouton afferent endings.* Most individual afferents in both zones contact both type I and type II HCs (“*dimorphic afferents*”). However, pure-calyx and pure-bouton individual afferents are respectively only found in the striola and extrastriola (Eatock and Songer, 2011; Goldberg, 2000). In amniotes there is no obligatory relationship between HC orientation reversal and zones. While the utricular striola is entirely medial to the LPR, the saccular striola is bisected by the LPR (Fig. 1A) (Deans, 2013; Li et al., 2008; Xue and Peterson, 2006). Moreover, central and peripheral zones of cristae bear many anatomical and physiological similarities to the striolar and extrastriolar zones, but cristae have no LPR and no abrupt variation in HC orientation, as in the organ of Corti.

Interestingly, mammalian otolith afferents have two distinct anatomical properties that segregate with the LPR. First, individual afferents are maximally excited by stimuli of one orientation and not the opposite (Fernandez et al., 1972; Goldberg et al., 1990), indicating that individual afferents selectively contact HCs sharing the same general orientation, as also observed in the zebrafish lateral line (Ji et al., 2018). Second, the central projections of afferent neurons innervating HCs on each side of the LPR are also distinct; afferents that innervate one HC orientation largely project to the cerebellum, while the opposite HC orientation projects to the brainstem (Ji et al., 2022; Maklad et al., 2010). The LPR thus

correlates with a striking segregation of both the peripheral and central projections of afferent neurons.

Recent work has illuminated how HCs with opposing orientations are formed during development (reviewed in (Tarchini, 2021)). Early in development all organs are polarized by core PCP proteins that are enriched asymmetrically at cell-cell junctions before HCs are born (Deans, 2013). In cristae, asymmetric core PCP proteins set up a default, uniform HC orientation across the epithelium. Because the asymmetric pattern of core PCP protein enrichment is unchanged across the LPR, a distinct, regional mechanism defines a HC population with an opposite orientation (Deans, 2013; Deans et al., 2007; Jones et al., 2014; Mirkovic et al., 2012). Regional expression of the transcription factor EMX2 in the lateral utricle and posterior saccule drives the 180°-reversed orientation of HCs compared to neighboring *Emx2*-negative HCs (Holley et al., 2010; Jiang et al., 2017). Although regionally restricted, *Emx2* is expressed by all cell types in the sensory epithelium. Reversal is achieved cell-autonomously in HCs by an orphan GPCR, GPR156 (Kindt et al., 2021). Unlike *Emx2*, *Gpr156* is transcribed throughout the sensory epithelia but is limited to HCs. In *Emx2*-positive HCs only, the GPR156 protein is trafficked and planar-polarized at apical junctions, where it signals through inhibitory G proteins to trigger a reversal in HC orientation. The EMX2>GPR156 reversal cascade is conserved in zebrafish neuromasts and loss of either of these proteins produces neuromasts where all HCs adopt the same, uniform orientation (Jacobo et al., 2019; Jiang et al., 2017; Kindt et al., 2021; Kozak et al., 2020; Lozano-Ortega et al., 2018).

Importantly, in addition to reversing HC orientation, Emx2 is required for afferent selectivity. In zebrafish *emx2* mutants, individual afferent fibers either innervate nearly all or very few HCs instead of innervating ~50% of HCs based on their shared orientation (Ji et al., 2018). In mouse otolith organs, regional *Emx2* expression is required for local afferents that innervate HC of one orientation to project centrally to the cerebellum and not to the brainstem (Ji et al., 2022). In zebrafish, Emx2 was also recently shown to affect HC mechanotransduction, thus defining an orientation-based functional asymmetry in lateral-line neuromasts (Chou et al., 2017; Kindig et al., 2023). It remains unknown

whether, similar to Emx2, GPR156 is required for orientation-based selectivity of afferent contacts in mouse otolith organs or zebrafish neuromasts, and whether Gpr156 participates in direction-based asymmetry of mechanosensitive response in neuromasts.

Here, using animal models where *Gpr156* is inactivated, we first established that abolishing the LPR in mouse otolith organs did not produce obvious changes in HC patterning and mechanotransduction properties. In contrast, we found that similar to Emx2, Gpr156 is required for asymmetric mechanotransduction in zebrafish neuromasts. Normal afferent segregation was maintained in both mice and zebrafish lacking GPR156 despite one HC population failing to reverse its orientation. Unchanged afferent organization in the mouse allowed us to specifically interrogate how the LPR serves vestibular function. We found that although *Gpr156* mutant mice did not show overt vestibular dysfunction, performance on two tests that engage otolith organs was significantly altered. This study clarifies how molecular mechanisms that orient HCs to achieve bi-directional sensitivity contribute to vestibular and lateral-line function.

170 RESULTS

171

172 **Normal hair cell numbers and organization in *Gpr156* mutant adult otolith organs**

173

174 In previous work (Kindt et al., 2021), we established that in sensory organs of the inner
175 ear and lateral-line, *Gpr156* expression is limited to HCs. In neonate otolith organs, we
176 demonstrated that GPR156 is required for EMX2-positive HCs to adopt a reversed
177 orientation compared to EMX2-negative HCs. We further showed that EMX2-positive HCs
178 lacking GPR156 do not correct their orientation with time and remain non-reversed in
179 young adults (P21-P28). Focusing on the utricular sensory epithelium, we showed normal
180 macular surface area and number of HCs in all three zones (LES, striola and MES; Fig.
181 1A) in adult *Gpr156*$^{del/del}$ mutants. Here we begin by extending our morphological
182 characterization of *Gpr156*$^{del/del}$ adult macular organs to include the saccule as well as
183 zonal and HC type profiles, before proceeding to functional and behavioral assessments.

184

185 We first verified that absence of GPR156 did not obviously interfere with striolar patterning
186 in adult animals. We used oncomodulin (OCM) to immunolabel striolar HCs (Simmons et
187 al., 2010) at 4-week of age (P28) and confirmed that striolar surface area and striolar HC
188 density were unaffected in constitutive *Gpr156*$^{del/del}$ mutant utricles and saccules
189 compared to controls (*Gpr156*$^{del/+}$; Fig. 1B-C). Each macular organ contains two main HC
190 types, type I and type II. Therefore, we next quantified type I HCs in the LES, striola and
191 MES zones of the adult utricle and in the anterior (ANT), striolar and posterior (POST)
192 zones of the adult saccule. We used SPP1/Osteopontin, a marker that labels the neck
193 region of approximately 90% of type I HCs (Fig. 1D-E) (McInturff et al., 2018). We
194 observed no difference in SPP1-positive type I HC numbers between mutants and
195 controls in any zone or organ (Fig. 1F). We next used a SOX2 antibody to label type II
196 HCs in the same zones (Fig. 1G-H). Again, we observed no difference in type II HC
197 numbers between mutants and controls (Fig. 1I). In summary, loss of GPR156 prevents
198 *Emx2*-positive HCs from reversing their orientation but does not affect macular patterning,
199 including division into clear zones and appropriate numbers of type I and type II HCs
200 throughout.

201

202 **No defects in mechano-electrical transduction were detected in individual mouse**
203 **utricular hair cells of *Gpr156* mutants**

204

205 After establishing normal numbers and types of mouse vestibular HCs, we assessed
206 whether HCs respond normally to hair bundle deflections in the absence of GPR156. For
207 this assessment, we recorded whole-cell mechano-electrical transduction (MET) currents
208 of HCs in the utricle of *Gpr156*$^{del/del}$ mutants. To stimulate transduction, we deflected
209 individual mechanosensory hair bundles of HCs from *Gpr156*$^{del/del}$ mutants and
210 heterozygous *Gpr156*$^{del/+}$ control utricles with a rigid probe coupled to the back (short
211 edge) of the bundle (see Methods, Fig. 2A). All bundles were positively deflected along
212 their orientation axes. I_{MET} recordings were taken between P8 and P100 (median age for
213 comparisons: ~P20 for both null and heterozygous genotypes; see Tables).

214

215 We first compared properties of the evoked MET current (I_{MET}) across genotypes in the
216 LES, the zone in which hair bundles fail to reverse in *Gpr156* mutants. ~70% (93/135) of
217 LES HCs responded with detectable I_{MET} (within 20 pA) to hair bundle deflection,
218 regardless of HC type and genotype (Chi-squared test, Table 1). We attribute the
219 insensitivity of the remaining cells to damage during dissection of the tissue, given that
220 damaged bundles can be seen in every preparation, zone, and bundle type, independent
221 of genotype.

222

223 I_{MET} responses are shown for families of iterated 400-ms steps of displacement; subsets
224 of these families are shown in Fig. 2B-E. During bundle displacement, I_{MET} typically
225 peaked at step onset. As noted before (Vollrath and Eatock, 2003), traces evoked by
226 stimuli in the middle of the operating range adapted with a time course fit by 1-2 decaying
227 exponential terms. Because type I and II HCs were voltage-clamped at different holding
228 potentials (V_{hold} = –94 and –84 mV, respectively, see Methods), their MET currents
229 experienced different driving forces. We normalized for driving force by converting current
230 to conductance (G) and plotted G as a function of hair bundle displacement (X) for each
231 HC type and genotype (Fig. 2F-G). G(X) curves were fit with a simple Boltzmann function

232 (Eq. 1, Methods), yielding values for maximum conductance (G_{max}), the midpoint of the
233 G(X) curve ($X_{1/2}$, displacement at half-maximal I_{MET}) and *dx* (slope factor), the
234 displacement range corresponding to an e-fold increase in G for small displacements.
235 Among the LES HCs tested, no significant differences were detected between genotypes
236 for any Boltzmann parameter (G_{max}, $X_{1/2}$, or *dx*) (Fig. 2F-G, Table 2). G_{max} values were in
237 the range of 2.5-3.0 nS, $X_{1/2}$ was 200-300 nm and *dx* was 150-200 nm (Table 2). From
238 G(X) relations we estimated the operating range (OR; displacement range yielding 10-
239 90% growth of G_{MET}) to be ~800-900 nm for all LES HCs (Table 2). In summary, the peak
240 (non-adapted) displacement sensitivity of I_{MET} was not detectably affected in LES hair
241 bundles of mutants.
242
243 Another salient feature of vestibular HC transduction is adaptation (response decay)
244 during a steady hair bundle deflection. We fit the adaptation with one or more exponential
245 decays, and also calculated its extent (% decay) (Eq. 4, Methods; Fig. 2B-E). As reported
246 previously for immature mouse utricular HCs (Vollrath and Eatock, 2003), these mature
247 mouse utricular HCs had fast and slow adaptation components. The fast component was
248 more prominent at small displacements and the slow component dominated at large
249 displacements; often, both were evident in the middle of the operating range. We
250 therefore compared adaptation time constants, τ_{fast} and τ_{slow}, at the midpoint of the
251 operating range ($X_{1/2}$). For 400-ms steps, mean values are in the range of 4 - 10 ms and
252 70 – 140 ms, respectively, and the two components are responsible for comparable
253 extents of the total adaptation. These results are consistent with previous reports with
254 similar methods from immature mouse utricular HCs (Vollrath and Eatock, 2003) and
255 immature rat saccular HCs (Songer and Eatock, 2013. In the current sample, however,
256 adaptation at $X_{1/2}$ included a significant third, faster adaptation component ("very fast";
257 τ_{VF} < 1 ms) in most type I HCs (12/13) and 2/10 type II HCs. In the LES, we detected no
258 significant differences with genotype in adaptation rates or extent (Table 2).
259
260 **No changes were detected in voltage-gated conductances of individual mouse**
261 **utricular hair cells of *Gpr156* mutants**
262

263 MET current initiates the receptor potential, which in turn modulates substantial voltage-
264 gated currents in the HC's basolateral membrane, especially K^+ currents, which further
265 shape the receptor potential. For example, type I HCs make relatively fast, small receptor
266 potentials compared to type II HCs because type I HCs have many more K channels that
267 are open around resting potential. To test for effects of *Gpr156* deletion on voltage-
268 dependent currents, we applied voltage step protocols to whole-cell clamped type I and
269 type II HCs in the LES of *Gpr156*$^{del/del}$ and *Gpr156*$^{del/+}$ utricles (Fig. 3A-D).
270
271 The time course and voltage dependence of outwardly rectifying voltage-gated current
272 from LES type I cells of *Gpr156*$^{del/del}$ utricles resembled those of *Gpr156*$^{del/+}$ utricles (Fig.
273 3A, C). Most of the current in type I HCs (Fig. 3A, C) flows through a low-voltage-activated
274 K^+ conductance ($g_{K,L}$) that dominates the type I HC voltage response. As described in
275 Methods, we used the current data to generate conductance density vs. voltage (G/Cm -
276 V) curves (Fig. 3E) and fitted them with the Boltzmann function (Eq. 5, Methods) to show
277 how the open probability of $g_{K,L}$ varies with voltage. In both genotypes, approximately half
278 of $g_{K,L}$ was activated at resting membrane potential, V_{rest} (~–85 mV). As a consequence
279 of their large K^+ conductance at V_{rest}, type I cells had low input resistances (R_{in} ~50 MΩ).
280 As is typical of type I HCs, the maximal K^+ conductance density (G_{max}/C_m), which is
281 proportional to the maximal number of open channels per unit membrane area, was much
282 larger than for type II HCs (Fig. 3E vs. 3F, note difference in conductance scale; Table 3).
283
284 Similarly, we detected no effect of genotype on the voltage-dependent outward currents
285 of LES type II HCs (Fig. 3B, D, F). The currents activated positive to resting potential (~–
286 72 mV) and had activation midpoints ($V_{1/2}$ values) of –30 to –40 mV. Because of the small
287 voltage-gated conductance at rest, input resistance was ~10-fold higher than in type I
288 HCs (~500 MΩ vs. ~50 MΩ). The outward currents inactivated significantly within 400 ms,
289 indicating a substantial A-current component. The maximum conductance density
290 (G_{max}/C_m) at 400 ms (~steady state), which is proportional to the number of open channels
291 per unit membrane area, was much smaller than in type I HCs. Again, no effect of
292 genotype was detected on the differences between type I and II HCs of the LES (Table
293 3).

294

295 Together these results are consistent with previous reports on key physiological
296 properties of type I and II HCs in amniote vestibular organs. The mature physiological
297 status of each HC type appeared to be preserved in LES HCs that failed to reverse their
298 orientation because GPR156 was inactivated.

299

300 **Hair cell physiology beyond the lateral extrastriolar domain: Variations in**
301 **properties were not related to loss of GPR156**

302

303 Loss of GPR156 does not impact HC orientation in the striola and MES, but *Gpr156* is
304 transcribed in all HCs across the maculae (Kindt et al., 2021). We thus investigated
305 transduction and adaptation in those zones as well (Fig. 4). While there was heterogeneity
306 across HCs, we saw no striking systematic differences with genotype in the voltage-gated
307 or mechanotransduction currents from control *vs. Gpr156* mutants (but note that the
308 statistical power of the comparisons is low, Table 4).

309

310 **Gpr156 impacted the mechanosensitive properties of lateral-line hair cells in**
311 **zebrafish**

312

313 Similar to otolith organs of mammals, each neuromast within the posterior lateral-line
314 system of zebrafish has two populations of HCs that enable the detection of anterior- or
315 posterior-directed fluid flow (Fig. 5A). To allow bi-directional detection, both Emx2 and
316 Gpr156 are required to reverse the orientation of one HC population so that it can detect
317 posterior flow (Fig. 5A) (Jiang et al., 2017; Kindt et al., 2021). Previous work has shown
318 that in wild-type animals, the mechanosensitive properties of HCs that detect anterior flow
319 (Emx2^{-}) are larger compared to those that detect posterior flow (Emx2^{+}) (Kindig et al.,
320 2023). Further, this work demonstrated that loss or gain of Emx2 in all lateral-line HCs
321 was able to not only alter HC orientation, but also increase and decrease
322 mechanosensitive responses respectively (Kindig et al., 2023). Our current results in the
323 mouse utricle did not detect significant differences in the mechanotransduction properties

324 of HCs lacking GPR156 (Fig. 2). Whether loss of Gpr156 alters the mechanosensitive
325 properties of lateral-line HCs is not known.
326
327 To address this question, we used a membrane-localized GCaMP6s reporter in HCs
328 (memGCaMP6s) (Kindt et al., 2021) to perform *in vivo* calcium imaging (Lukasz and Kindt,
329 2018) and. By imaging GCaMP6s signals in an apical plane containing the hair bundles,
330 we measured evoked, mechanosensation-dependent calcium signals during fluid-jet
331 stimulation. We used this approach to stimulate in both the anterior and posterior direction
332 and compared the magnitude of the mechanosensitive responses in lateral-line HCs in
333 both control (*gpr156*$^{+/-}$*)* and *gpr156* mutants. As shown previously, we could reliably
334 identify the orientation (ANT vs POST) among control HCs using this approach (eg: Fig.
335 5B). We first verified that in control animals, the magnitude of the mechanosensitive
336 responses of HCs that detect anterior flow was greater than those that detect posterior
337 flow (eg: Fig. 5B and Fig. 5D, F). Consistent with previous work, in *gpr156* mutants, we
338 found that the majority of HCs only responded to anterior flow (eg: Fig. 5C) (Kindt et al.,
339 2021). Importantly, we found that the magnitude of the mechanosensitive responses in
340 *gpr156* mutants was not different when compared to control HCs that respond to anterior
341 flow (eg: Fig. 5C and Fig. 5E-F). Further, the mechanosensitive responses in *gpr156*
342 mutants were significantly larger than control HCs that respond to posterior flow (Fig. 5F).
343
344 Our analysis thus indicates that in *gpr156* mutants, lateral-line HCs show larger
345 mechanosensitive responses. These responses are similar to HCs in control animals that
346 respond to anterior flow (Emx2^{-}). Together, this data suggests that the EMX2-GPR156
347 mechanism driving HC orientation reversal also affects HC transduction in zebrafish
348 neuromasts.
349
350 **Segregated afferent receptive fields were preserved in mouse utricles lacking**
351 **GPR156**
352
353 After characterizing the functional properties of HCs in mouse and zebrafish *Gpr156*
354 mutants, we examined whether GPR156 plays a role in orientation-selective afferent

355 innervation. Previous work has demonstrated that *Emx2* expression in the LES of the
356 mouse utricle and in HCs that sense posterior flow in the lateral line is required for
357 afferents to innervate HCs of similar (rather than opposing) orientation (Ji et al., 2022; Ji
358 et al., 2018). Whether GPR156 plays a similar role in direction-selective afferent
359 innervation is unknown.
360
361 To investigate whether afferent organization in the LES is disrupted by loss of GPR156,
362 we first compared the terminal fields of individual dye-filled calyx-bearing afferents in
363 *Gpr156*$^{del/+}$ *and Gpr156*$^{del/del}$ utricles. All LES calyces belong to dimorphic afferents, which
364 form both calyces on type I HCs and boutons on type II HCs. To examine terminal fields,
365 a fluorescent internal solution was injected into a calyx terminal within the LES during
366 whole-cell recordings. The fluorescent dye was then allowed to diffuse into the calyx and
367 from there throughout the terminal arbor.
368
369 Using this approach, we found that terminal arbors (receptive fields) in *Gpr156*$^{del/+}$ control
370 utricles (n = 12) comprised 1 or 2 calyces and as many as 65 boutons (median: 29) (Fig.
371 6A-C). The labeled afferent terminals were restricted to LES in all but one case (Fig. 6A).
372 In this single case, a terminal branch crossed the LPR, innervating 16 striolar HCs with
373 opposite orientation to the 12 LES HCs also innervated. In some filled LES afferents, a
374 thin branch originated below the epithelium (Fig. 6C, Supplemental video 1), as previously
375 described for chinchilla extrastriola (Fernandez et al., 1990). We also labeled a single
376 striolar calyx from a control utricle near the striolar/MES boundary; its terminal field was
377 excluded from the calbindin-negative MES (Fig. 6D).
378
379 When we performed dye labeling in *Gpr156*$^{del/del}$ utricles, the innervation patterns and the
380 size of terminal fields appeared similar to *Gpr156*$^{del/+}$ controls. In *Gpr156*$^{del/del}$ utricles, the
381 labeled LES afferents (n = 8) were also all dimorphic, terminating in up to three calyces
382 and 56 boutons (median: 23). The labeled receptive fields did not cross the striola/LES
383 border (Fig. 6E-G). We also did not observe fiber branches extending across the border
384 from parent axons (Fig. 6E-G; Supplemental video 2). As observed in the lone *Gpr156*$^{del/+}$
385 striolar afferent (Fig. 6D), *Gpr156*$^{del/del}$ afferents with the main dendritic fiber terminating

386 in the striola (n = 4) contacted relatively few HCs, and receptive fields were restricted to
387 the calbindin-positive region (Figure 6H).
388
389 To confirm and complement dye-filling results at the whole organ level, we used a new
390 genetic approach to specifically label afferents innervating EMX2^{+} HCs in the LES.
391 Interestingly, when breeding the *Advillin-Cre* strain (Zhou et al., 2010) with the *Tigre Ai140*
392 reporter (Daigle et al., 2018), we only observed Cre recombination and EGFP expression
393 in vestibular ganglion neurons that contacted HCs in the lateral utricle region (Fig. 7A).
394 Close examination revealed clear labeling of HC calyces in the LES, and occasionally in
395 OCM^{+} HCs in the lateral striola (Fig. 7B, arrowheads). We confirmed that similar to OCM^{-}
396 EGFP^{+} HCs in the LES, these OCM^{+} EGFP^{+} HCs were invariably oriented towards the
397 medial edge (Fig. 7C). This demonstrated that *Advillin* expression defines a population of
398 neurons whose peripheral processes closely segregate with HC orientation, irrespective
399 of striolar (OCM^{+}) or extrastriolar (OCM^{-}) HC identity. Importantly, HC innervation by
400 *Advillin*-positive neurons was unchanged in *Gpr156*$^{del/del}$ mutants (Fig. 7A-B). We
401 observed equivalent numbers of OCM^{+} HCs innervated in the lateral striola in *Gpr156*$^{del/del}$
402 mutants compared to controls (Mann-Whitney p=0.74; average OCM^{+}/EGFP^{+} HCs per
403 utricle: *Gpr156*$^{del/+}$: 20.25, *Gpr156*$^{del/del}$:19.25; 3 animals and 4 utricles per genotype; no
404 OCM^{+}/EGFP^{+} HCs oriented towards the lateral edge were recorded in either genotype).
405
406 In summary, we detected no anomaly in afferent receptive fields in utricles lacking
407 GPR156 and thus lacking a LPR, showing that the tendency of afferents to innervate HCs
408 on one side of the LPR is not controlled by GPR156 or HC orientation.
409
410 **Afferent firing patterns were preserved in mouse utricles lacking GPR156**
411
412 Our innervation data suggested that HCs in zones demarcated by the LPR are still
413 innervated by distinct populations of afferent neurons in *Gpr156*$^{del/del}$ mutants. We next
414 investigated whether the LES afferent population retains normal physiology. Striolar
415 afferents have highly irregular inter-spike intervals, while extrastriolar afferents in both
416 LES and MES have much more regular inter-spike intervals (Goldberg, 1991; Goldberg,

417 2000; Goldberg et al., 1990). Associated with the difference in spike timing regularity are
418 zonal differences in response dynamics and information encoding capacity (e.g., (Jamali
419 et al., 2019)). The spike timing difference is considered to reflect differences in afferents'
420 excitability as conferred by their intrinsic ion channels, with regular afferents being more
421 excitable (Kalluri et al., 2010; Ventura and Kalluri, 2019). To test for effects of *Gpr156*
422 inactivation on afferent excitability, we injected small depolarizing current steps into LES
423 calyces through the whole-cell recording pipette and measured current threshold for
424 spiking, I_{thresh}, and the numbers of spikes evoked by each current step.
425
426 As reported (Gonzalez-Garrido et al., 2021; Ono et al., 2020), I_{thresh} evoked 1-to-several
427 spikes but increments beyond I_{thresh} evoked more sustained firing (Fig. 8a-b). No
428 difference was observed across genotypes (Table 5): in both *Gpr156*$^{del/+}$ afferents (n=18)
429 and *Gpr156*$^{del/del}$ afferents (n=20), mean I_{thresh} was ~100 pA and ~95% of afferents
430 produced sustained spiking at $3\times I_{thresh.}$ These results suggest that afferent firing patterns,
431 and likely the underlying ion channel expression, are unaltered in the LES of *Gpr156*$^{del/del}$
432 utricles, despite abnormal HC orientation.
433
434 **Gpr156 was not required for afferent selectivity or synaptic pairing in zebrafish**
435 **lateral-line**
436
437 We next expanded our analysis to determine whether loss of Gpr156 impacts afferent
438 selectivity in the lateral-line. For this analysis we used mosaic expression of
439 *neuroD:tdTomato* to label single lateral-line afferent neurons. After identifying *gpr156*
440 mutant and control *(gpr156*$^{+/-}$) animals with labeled fibers, we immunolabeled to visualize
441 orientation (phalloidin), HC bodies (MYO7), and cell type (presence or absence of Emx2).
442 We then used confocal microscopy to image the innervation pattern of single afferents.
443
444 Consistent with previous results, some afferent fibers selectively contacted Emx2^{-} HCs
445 with hair bundles oriented to respond to anterior flow in control animals (Fig. 9A-H). Other
446 afferent fibers selectively contacted Emx2^{+} HCs with hair bundles oriented to respond to
447 posterior flow (Supplemental fig. 1A-H). We then examined the innervation patterns of

448 afferent fibers in *gpr156* mutants. Similar to controls we were able to identify fibers with a
449 clear preference for Emx2$^-$ or Emx2$^+$ HCs (Fig. 9I-P, Supplemental fig. 1I-P). Importantly,
450 in *gpr156* mutants, afferent fibers innervated HCs based on the presence or absence of
451 Emx2, despite all HCs responding to anterior flow.
452
453 Following this initial assessment, we quantified the percentage of HCs per neuromast that
454 were innervated by each afferent fiber. We found that *gpr156* mutant fibers innervated a
455 similar percentage of HCs per neuromast compared to controls (Fig. 9Q, control: 38.90 %
456 ± 2.40, n = 18, *gpr156* ko: 41.31 % ± 2.33, n = 23, p = 0.48). We also quantified how
457 selective each afferent fiber was for Emx2$^+$ or Emx2$^-$ HC. For each afferent fiber, we
458 calculated the percentage of either Emx2$^+$ or Emx2$^-$ HCs innervated out of the total
459 number of innervated HCs. In both control and *gpr156* mutants, afferent fibers showed a
460 high selectivity (Fig. 9R, control: 85.06 % ± 4.32, n = 18, *gpr156* ko: 81.29 % ± 3.17, n =
461 23, p = 0.48). We split this dataset and examined the selectivity of afferent fibers that
462 preferentially contacted either Emx2$^-$ or Emx2$^+$ HCs (Fig. 9S-T). This analysis revealed
463 that in control and *gpr156* mutants, both afferent fiber types were highly selective
464 (afferents contacting Emx2$^-$ cells, control: 81.41 % ± 7.90, n = 8, *gpr156* ko: 79.37 % ±
465 4.73, n = 10, p = 0.82; afferents contacting Emx2$^+$ cells, control: 87.99 % ± 4.75, n = 10,
466 *gpr156* ko: 82.80 % ± 4.38, n = 13, p = 0.43). Overall, our single fiber labeling revealed
467 that Gpr156 is not required for afferent fibers to selectively innervate HCs based on the
468 presence or absence of Emx2.
469
470 To extend this analysis, we examined synaptic pairing in *gpr156* mutants. Previous
471 research found that along with inappropriate innervation, there is an increase in the
472 amount of unpaired pre- and post-synapses in *emx2* mutants (Ji et al., 2018). We
473 immunostained control along with *gpr156* and *emx2* mutant HCs with Ribeye b to label
474 presynapses and pan-MAGUK to label postsynapses (Fig. 10A-C). We then quantified
475 the number of complete immunolabeled synapses per HC. Among all genotypes, the
476 number of complete synapses was unaltered (Fig. 10D, control 3.56 ± 0.06, n = 9
477 neuromasts, *gpr156* ko: 3.61 ± 0.10, n = 16 neuromasts, p = 0.74; control 3.51 ± 0.27, n
478 = 9 neuromasts, *emx2* ko: 3.67± 0.08 n = 9 neuromasts, p = 0.50). We also quantified

479 unpaired pre- and post-synapses. Similar to previous results, there were more unpaired
480 pre- and post-synapses per neuromast in *emx2* mutants compared to controls (Fig. 9E-
481 F, presynapses, *emx2*$^{+/+}$ or *emx2*$^{+/-}$ control 2.00 ± 0.53, n = 9 neuromasts, *emx2* ko: 4.22
482 ± 0.70, n = 9 neuromasts, p = 0.02; postsynapses, control 1.44 ± 0.56, n = 9 neuromasts,
483 *emx2* ko: 6.56 ± 0.78, n = 9 neuromasts, p < 0.0001). In contrast, in *gpr156* mutants,
484 there was no increase in unpaired pre- or post-synapses per neuromast compared to
485 controls (Fig. 10E-F, presynapses, *gpr156*$^{+/-}$ control 2.11 ± 0.31, n = 9 neuromasts,
486 *gpr156* ko: 1.68 ± 0.23, n = 16 neuromasts, p = 0.29; postsynapses, control 0.33 ± 0.17,
487 n = 9 neuromasts, *gpr156* ko: 0.75 ± 0.17, n = 16 neuromasts, p = 0.12). A lack of unpaired
488 pre- and post-synapses in *gpr156* mutants further confirms that Emx2 but not Gpr156
489 impacts afferent innervation in lateral-line HCs.
490
491 In summary, *Gpr156* inactivation does not appear to impact afferent selectivity in either
492 mouse or zebrafish. This is in sharp contrast with results in *Emx2* mutants, where
493 orientation-specific HC afferent innervation is profoundly altered in mouse and zebrafish
494 (Ji et al., 2022; Ji et al., 2018). It follows that HC orientation per se does not dictate afferent
495 selectivity, with EMX2 likely using a different effector(s) than GPR156 in this context. Thus,
496 afferent studies confirm that the *Gpr156*^{del} model is well-suited to investigate specifically
497 how the reversal of HC orientation in otolith and lateral line organs serves organ function.
498
499 ***Gpr156* mutant mice had defects in otolith-driven, but not canal-driven, vestibular**
500 **behaviors**
501
502 In mammals, only otolith organs (utricle, saccule) have a LPR. Therefore, the absence of
503 a LPR in *Gpr156* mutants should only affect otolith-driven reflexes and behaviors. In order
504 to test this prediction we compared *Gpr156* control and mutant mice on a number of tests
505 that can discriminate between otolith and canal inputs.
506
507 <u>Normal posture, balance beam but impaired swimming performance in *Gpr156* mutants</u>
508 To assess how loss of the LPR affects vestibular functions, we first determined whether
509 *Gpr156* mutant mice showed postural/balance impairments. Visual and quantitative

510 assessments did not reveal circling or head tremor behaviors in *Gpr156*$^{del/del}$ mice at rest
511 (Supplemental fig. 2). Additionally, we conducted basic standard behavioral tests that
512 involve subjective scoring: (1) tail hanging, (2) air righting, and (3) contact inhibition of
513 righting. Both control and *Gpr156*$^{del/del}$ mice scored 0 (where 0=normal, see Methods) on
514 each of these behavioral tests (Supplemental fig. 3A-C).
515
516 After this initial assessment, we next subjected mice to more challenging balance tests
517 including walking along a narrow balance beam and swimming. On the balance beam,
518 both *Gpr156*$^{del/del}$ and *Gpr156*$^{del/+}$ mice showed normal coordination (Fig. 11A). However,
519 when *Gpr156*$^{del/del}$ mice were placed in water, they demonstrated severely impaired
520 swimming compared to *Gpr156*$^{del/+}$ controls. This impairment was characterized by
521 underwater tumbling and the inability to maintain normal upright posture in the water. All
522 mice were rescued within 60 seconds and the average time of rescue was significantly
523 lower in *Gpr156*$^{del/del}$ compared to control mice (Fig. 11B; *Gpr156*$^{del/+}$ controls= 49.9±3.0s;
524 *Gpr156*$^{-del/del}$= 17.4±2.7s; P<0.0001). Overall, these results indicated that GPR156 is
525 required for vestibular function important for swimming behavior.
526
527 We hypothesized that markedly impaired swimming performance could be due to deficits
528 in the otolith rather than semicircular canal dependent pathways. To test this proposal,
529 we quantified eye movements generated by two different vestibulo-ocular reflex
530 behaviors, one driven by activation of the semicircular canals (angular vestibular-ocular
531 reflex, or angular VOR) and the other driven by activation of the otoliths (off-axis vertical
532 rotation, or OVAR).
533
534 <u>Normal aVOR and OKR responses in *Gpr156* mutants</u>
535 We first quantified the angular vestibulo-ocular reflex in *Gpr156*$^{del/del}$ and *Gpr156*$^{del/+}$
536 control mice in darkness (VORd). The angular VOR was evoked by rotating the animal
537 sinusoidally around earth vertical axis. To quantify the angular VORd we computed the
538 gain and phase for each testing frequency (0.2, 0.4, 0.8, 1, and 2Hz, ±16°/s). During
539 VORd, both control and *Gpr156*$^{del/del}$ mice displayed robust compensatory eye
540 movements, which increased as a function of frequency (Fig. 12A-B). Further, to confirm

541 that there was no visual deficit in *Gpr156*$^{del/del}$ mice, we also tested their optokinetic reflex
542 (OKR) by rotating a patterned visual surround sinusoidally about earth vertical axis at
543 the same testing frequencies, while the animal remained stationary (see Methods). The
544 OKR responses of *Gpr156*$^{del/del}$ and control mice were comparable, confirming that there
545 was no visual deficit in *Gpr156* mutants (Fig. 12C-D). For the sake of completeness, we
546 quantified the angular VOR evoked in the light (VORl) by rotating the animal sinusoidally
547 around earth vertical axis, while the patterned visual surround remained stationary.
548 Again, we found no difference in the VORl response of *Gpr156*$^{del/del}$ versus control mice
549 in this lit environment (Figure 12E-F). Finally, we tested whether *Gpr156*$^{del/del}$ mice
550 demonstrated normal ability to adapt their angular VOR. We used a standard angular
551 VOR motor learning protocol (see Methods) in which we carried out 30-minute-long VOR
552 gain-down training for both control and *Gpr156*$^{del/del}$ mice. Head restrained mice were
553 rotated with the visual surround in phase. The training stimulus was 2 Hz with a peak
554 velocity of 16°/s. The learning efficacy was assessed by quantifying change in the VOR
555 gain after training. In both control and *Gpr156*$^{del/del}$ mice, this VOR motor learning
556 protocol produced a significant reduction in VOR gain after training (Supplemental fig.
557 4A-B). Overall, *Gpr156*$^{del/del}$ and control mice demonstrated a comparable percent
558 change of gain decrease at each testing frequencies (Supplemental fig. 4C). Together,
559 our VOR and OKR results indicated normal semicircular canals-driven responses in
560 *Gpr156*$^{del/del}$ mice.
561
562 <u>Altered OVAR responses in *Gpr156* mutants</u>
563 As no defects were apparent in semicircular canal-mediated behavior, we next tested
564 whether otolith-mediated vestibulo-ocular reflex behaviors were impaired in *Gpr156*$^{del/del}$
565 mice. For this assessment, we recorded eye movements while the mouse was tilted 17°
566 off-the vertical axis (i.e., off-vertical axis rotation (OVAR)), and then rotated at a constant
567 velocity (50°/s for 72 sec). The eye velocity evoked by this paradigm comprised two
568 different responses: (1) a transient canal-mediated response that decayed over the first
569 10-15 sec and (2) an otolith-mediated steady-state response in which eye velocity
570 oscillated around a constant bias with a sinusoidal waveform (Figure 12G). Overall, our
571 analysis revealed that transient OVAR responses did not differ between control and

572 *Gpr156*$^{del/del}$ mice, supporting the proposal that absence of GPR156 did not affect canal-
573 related ocular responses. In contrast, steady-state OVAR responses demonstrated a
574 significantly impaired bias in *Gpr156*$^{del/del}$ mice as compared to controls (Figure 12G-H).
575 The OVAR of *Gpr156*$^{del/del}$ mice was characterized by a significantly reduced bias relative
576 to controls (*Gpr156*$^{del/del}$: bias=0.039 ± 0.26 versus control: bias=3.85 ± 0.54, P = 4.03E-
577 5). Thus taken together, these results show that the absence of HC reversal in
578 *Gpr156*$^{del/del}$ alters otolith-mediated OVAR responses. This in turn may explain the
579 swimming deficits observed (Fig. 11B).
580
581
582

583 **DISCUSSION**

584

585 **Hair bundle orientation vs. zonal identity**

586 Taken together, our observations in utricles lacking GPR156 agree with other evidence
587 that in mouse vestibular epithelia, HC orientation is controlled separately from other
588 zonally differentiated properties of either HCs or afferents. Prior evidence includes data
589 from *Emx2* knockouts also exhibiting loss of the LPR without altering zoning (Jiang et al.,
590 2017) and data showing that inactivating a retinoic acid dehydrogenase deletes striolar
591 identity without affecting HC orientation (Ono et al., 2020). This conclusion stands in
592 contrast to zebrafish lateral line results, where transduction properties vary with HC
593 orientation depending on Emx2 (Kindig et al., 2023) and Gpr156 (this study).

594

595 **Asymmetrical mechano-electrical transduction**

596 Zebrafish lateral-line HCs use a combination of 2 mechanosensitive channels, Tmc2a
597 and Tmc2b (Chou et al., 2017). In the posterior lateral line, Emx2^{+} HCs that sense
598 posterior flow rely on primarily on Tmc2b, while Emx2^{-} HCs that sense anterior flow rely
599 on both Tmc2a and Tmc2b. Recently, a functional asymmetry was discovered between
600 anterior- and posterior-sensitive HCs: Emx2^{+} HCs that rely primarily on Tmc2b have
601 smaller mechanosensitive responses compared to Emx2^{-} HCs that rely on both Tmc2a
602 and Tmc2b. (Kindig et al., 2023). This work raises the possibility that the transcription
603 factor Emx2 inhibits *tmc2a* transcription to reduce mechanosensitive responses in HCs
604 sensing posterior flow. In our present study we find that functional asymmetry was also
605 lost in *gpr156* mutants (Fig. 5). In the context of mouse HC orientation, EMX2 is necessary
606 and sufficient to enrich and polarize GPR156 at HC apical junctions and reverse HC
607 orientation (Kindt et al., 2021). As the Gpr156 receptor is unlikely to act transcriptionally,
608 zebrafish Emx2 may act through Gpr156 to impact Tmc2a/2b function. For example,
609 polarization of Gpr156 at apical junctions may limit scaffolding or transport of Tmc
610 proteins to homomeric channels composed of Tmc2b. Overall, our work in zebrafish
611 indicates that both Emx2 and Gpr156 are important to dictate HC orientation and the
612 mechanosensitive properties of HCs with opposing orientations.

613

614 We did not see a clear impact of GPR156 loss on the transduction properties of *Emx2*$^{+}$
615 HCs in the mouse utricle (Fig. 2-4). Subtle effects remain possible given the natural
616 variance in the data and low power of the negative results. Nevertheless, current results
617 suggest normal HC function in the *Gpr156* mouse mutant, a prerequisite to interrogate
618 how non-reversed HCs affects vestibular behavior.
619
620 **Importance of the LPR for vestibular function**
621 The brain combines information from the maculae and cristae with inputs from other
622 modalities, including the somatosensory and visual systems, to compute a representation
623 of our self-motion and spatial orientation (reviewed in (Cullen, 2019). Our present findings
624 demonstrate that GPR156 is *not* required for macular HCs to selectively contact different
625 afferents across the LPR. Accordingly, we predicted that HCs that fail to reverse in the
626 lateral utricle of *Gpr156* mutants would lead to deficits in paradigms that test macular
627 contributions to behavioral responses. Indeed, *Gpr156* mutant mice demonstrated
628 impaired performance on two tests that engage the otolith organs: swimming and off-
629 vertical-axis rotation (OVAR). First, during swimming, impaired spatial orientation results
630 from the combined altered otolith input and reduced somatosensory feedback due to the
631 aqueous environment. Second, *Gpr156* mutant mice displayed impaired sustained
632 responses to off-vertical axis rotation (OVAR). While initial eye movement response to
633 OVAR is mediated by stimulation of semicircular canal HCs, the canal response decays
634 such that sustained eye movement is solely driven by the otolith stimulation (Beraneck et
635 al., 2012; Ono et al., 2020). Quantification of the sustained responses revealed a marked
636 reduction in this otolith-mediated reflex response. Confirming that these deficits are
637 specific to otolith function, the *Gpr156* mutant mice did not show overt vestibular
638 dysfunction such as spinning or head tilt that can arise with global dysfunction of
639 vestibular epithelia. Further, they displayed normal performance during testing that
640 selectively engaged superior canal organs, namely angular VOR in the light and dark.
641 This latter finding was predicted; because HC orientation is unchanged in *Gpr156* mutant
642 cristae, the coding properties of semicircular canal afferents should be unchanged and
643 would therefore produce a normal angular VOR upon specific stimulation of canal
644 ampullae.

645

646 **Comparing vestibular phenotypes of *Gpr156* and *Emx2* mutants**

647 *Gpr156* does not appear to be significantly expressed in the central nervous system
648 according to the Allen Brain Atlas (Lein et al., 2007). In addition, *Advillin-Cre* tracing and
649 dye-filling experiments (Fig. 6-7) showed that vestibular ganglion neurons still selectively
650 innervated LES HCs even when lacking GPR156. We thus speculate that HC signals in
651 the LES zone of *Gpr156* mutants are relayed to the cerebellum (Ji et al., 2022; Maklad et
652 al., 2010) via the central projection of *Advillin*$^{+}$ neurons as usual, but with abnormal (non-
653 reversed) response polarity. Overall, it appears unlikely that vestibular deficits observed
654 in our constitutive *Gpr156* mouse mutants reflect defective neuronal activity in addition to
655 a missing LPR. That said, we cannot entirely rule out another role of GPR156 beside its
656 regulation of HC orientation. This could be addressed in a follow-up study by limiting
657 *Gpr156* inactivation to HCs.

658

659 It is interesting to compare vestibular-related behaviors between the *Gpr156* and *Emx2*
660 mouse models in light of established similarities and differences in protein distribution and
661 function (Ji et al., 2022; Jiang et al., 2017; Kindt et al., 2021). Regarding behavior, this
662 study and work by Ji et al., 2022 agree that vestibular deficits in each model are relatively
663 mild (normal balance beam, VOR and OKR). *Emx2* inactivation in HCs (*Gfi1-Cre*) showed
664 impaired swimming ability, but defects were less severe and different in nature compared
665 to constitutive *Gpr156* mutants. *Gpr156* mutants displayed substantial difficulty in
666 maintaining their orientation in water, and frequently rolled over such that they needed to
667 be rescued. In contrast, *Emx2* mutants did not need rescue and were described as
668 demonstrating “frantic” swimming behavior, spending more time trying to climb out of the
669 water as compared to their littermate controls. OVAR highlighted otolith-specific defects
670 in *Gpr156* mutants but was not performed in *Emx2* mutants.

671

672 GPR156 acts downstream of EMX2 to regulate hair bundle orientation, and perhaps
673 mechanosensitivity in zebrafish. Another significant new result in the current study is to
674 show that afferent projections segregate with HC orientation and not with zonal identity
675 (Fig. 7; Advillin neuron labeling), yet segregation does not depend on HC orientation since

676 it is unchanged in mouse and zebrafish *Gpr156* mutants (Fig. 6-10). It follows that EMX2
677 must influence afferent segregation (Ji et al., 2022; Ji et al., 2018) via other effectors
678 unrelated to HC orientation. Accordingly, Ji and colleagues concluded that EMX2
679 regulates HC orientation and afferent patterning independently, with *Emx2* expression in
680 support cells critical for proper afferent contacts with HCs (Ji et al., 2022). This aligns well
681 with previous evidence that *Gpr156* is only expressed in HCs (Kindt et al., 2021).
682
683 Ji and colleagues also used specific inactivation of the transduction protein TMIE in the
684 LES (*Emx2-Cre*) to silence the *Emx2*$^{+}$ HC population. Interestingly, as with *Emx2* mutants,
685 they did not observe severe behavioral defects, and swimming ability in particular was
686 not obviously compromised in contrast to *Gpr156* mutants. It should be noted however
687 that while the *Gpr156 KO* and *Emx2-Cre; Tmie cKO* models both lack a normal
688 complement of bidirectional responses, they provide different forms of aberrant linear
689 acceleration signals. In the *Tmie* cKO model, LES HC inputs to the cerebellum are
690 missing but in the *Gpr156* model they are retained and of opposite nature since LES HCs
691 fail to reverse their orientation.
692
693 Several considerations could potentially explain why the *Gpr156* model appears to display
694 more severe behavioral defects compared to the *Emx2* models. First, HC or afferent
695 properties were not tested in *Emx2* mutants (Ji et al., 2022) and may be defective. Second,
696 compounded HC orientation and afferent defects in the *Emx2* mutants could dampen the
697 deleterious consequence of having LES HCs drive a neuronal response of reversed
698 polarity. Afferent defects in *Emx2* mutants were reported during embryogenesis (E16.5)
699 and innervation could further degenerate in adults, further dampening the consequence
700 of non-reversed HC activity in the LES. It is worth noting that aberrant vestibular afferent
701 signals are clinically more deleterious than absent signals, which perhaps explains why
702 properly relayed yet aberrant signals from LES HCs in *Gpr156* mutants result in
703 behavioral defects worse than observed in *Emx2* or *Emx2-Cre; Tmie cKO* models.
704
705 In conclusion, the *Gpr156* mutant mouse model is well-suited to specifically interrogate
706 how HC orientation reversal and the resulting LPR influence vestibular function because

707 it appears to lack confounding afferent patterning defects. In future studies, this model
708 could be improved by limiting *Gpr156* inactivation to HCs.
709
710
711
712
713
714
715

716 **METHODS**

717

718 **Mouse strains and husbandry**

719 The *Gpr156*^{del} strain (*B6N(Cg)-Gpr156tm1.1(KOMP)Vlcg/J*; MGI:5608696) was produced
720 by the Knockout Mouse Project (KOMP) and studied previously in (Kindt et al., 2021).
721 The *Advillin-Cre* strain is *B6.129P2-Avil*$^{tm2(cre)Fawa/J}$ (MGI: 6196038) (Zhou et al., 2010).
722 The *Tigre Ai140* strain is *B6.Cg-Igs7*$^{tm140.1(tetO\text{-}EGFP,CAG\text{-}tTA2)Hze}$ (MGI: 5904001) (Daigle et
723 al., 2018). Some whole-cell patch clamp recordings were obtained from CD1 mice
724 (Charles River Laboratories USA). All animals were maintained in standard housing and
725 all animal work was reviewed for compliance and approved by the Animal Care and Use
726 Committees of The Jackson Laboratory (anatomical experiments), the University of
727 Chicago (cellular electrophysiology and afferent labeling experiments), and the Johns
728 Hopkins University School of Medicine (behavioral experiments).

729

730 **Mouse immunofluorescence and imaging (Figure 1, Figure 7)**

731 Temporal bones of adult animals were isolated, oval windows were cleared and the
732 cochlear apex was punctured to allow better access to the fixative. Samples were then
733 fixed in paraformaldehyde (PFA 4%) overnight at 4°C, rinsed in PBS and incubated
734 overnight in 4% Ethylenediaminetetraacetic acid (EDTA) at room temperature for
735 decalcification. Both the trio (utricle and crista) and the saccule were dissected from the
736 bone and their epithelium exposed. After dissection, samples were permeabilized and
737 blocked in PBS with 0.5% Triton-X100 and bovine serum albumin (1%) for at least at 1
738 hour at room temperature. For SPP1/Osteonpontin staining, temporal bones were
739 immediately dissected to isolate the trio and the saccule and expose their epithelium, and
740 an eyelash was used to scrape off the otoconia, Samples were then fixed in PFA 4% for
741 1h at room temperature before being permeabilized and blocked as described previously.
742 Primary and secondary antibodies were each incubated overnight at 4°C in PBS, and
743 fluorescent dye-conjugated phalloidin was added to secondary antibodies. Samples were
744 washed 3 times in PBS + 0.05% Triton-X100 after each antibody incubation before being
745 finally post fixed in PFA 4% for at least 1 hour at room temperature. Primary antibodies
746 used were:

747 Mouse anti-MYO7A (Developmental Studies Hybridoma Bank/DSHB 138-1, 1:1000)
748 Goat anti-OCM (Invitrogen, PA547832, 1:200)
749 Goat anti-SPP1 (R&D Systems, AF808, 1:200)
750 Rabbit anti-PCNT (Biolegend, PRB432C, 1:400)
751 Goat anti-SOX2 (R&D Systems, AF2018, 1:200)
752 Secondary antibodies used were raised in donkey and coupled with AlexaFluor (AF) 488,
753 555, or 647 (donkey anti-rabbit 488 (A-21206), donkey anti-mouse 647 (A-31571), donkey
754 anti-goat 555 (A-21432); Thermofisher Scientific). Fluorescent conjugated phalloidin was
755 used to reveal F-actin (CF405 (89138-126); Biotum).
756 Confocal images were captured on a line scanning confocal microscope (LSM8000) using
757 Zen 2.6 software, the Airyscan detector in confocal mode, and either a 20× or a 63× 1.4
758 NA oil objective lens (Carl Zeiss AG). Images show a single optical plane unless stated
759 otherwise in the figure legend.
760
761 **Mouse immunostain quantification (Figure 1, Figure 7)**
762 All images were processed using Adobe Photoshop (CC2020), and the same image
763 treatment was applied across genotypes for each experiment. All quantifications included
764 at least three animals of each genotypes, and all values plotted in the study, as well as
765 animal cohort size (N), HC number and stereocilia number (n) are detailed in legends. To
766 quantify striolar surface, striolar density, as well as HC Type I and II density by region,
767 images were captured using a DM5500B fluorescence microscope using the Leica
768 Application Suite (LASX) and a 20x objective (Leica). Striolar surface was measured
769 using the polygon selection and area tools in Fiji/ImageJ to define the striola based on
770 the Oncomodulin staining. Striolar density was measured by using the cell counter tool in
771 Fiji/ImageJ to obtain the total number of Oconmodulin positive HCs. That number was
772 then normalized by the total striolar surface previously measured to obtain a final number
773 of HCs per 1000μm^2. To measure Type I and Type II HC density by region, three regions
774 of interest (ROI) were defined centrally of either 130x50μm (utricle) or 150x40μm
775 (saccule). The lateral extrastriolar (LES) domain was placed 20μm inside the macula
776 starting from the lateral edge of the utricle, encompassing most of the region lateral to the
777 line of polarity reversal (LPR). The striolar domain was defined immediately adjacent to

778 the LES domain based on the LPR and oncomodulin signal in controls. The medial
779 extrastriolar (MES) domain started 50µm medial to the striolar domain. The anterior
780 extrastriolar domain (ANT) was placed 10µm from the anterior edge of the saccule. The
781 striolar domain was defined 20µm posterior to the ANT domain based on oncomodulin
782 staining in controls, and the posterior extrastriolar domain (POST) was defined 50µm
783 posterior to the striolar domain. The location of these domains is illustrated in Fig.1A. The
784 same fields and spacing were next used for the *Gpr156*$^{del/del}$ mutants. The cell counter
785 plugin in Fiji/ImageJ was used to count HCs in each ROI.
786
787 **Data analysis and statistics – mouse anatomy (Figure 1, Figure 7)**
788 All data were plotted in Prism 9 (GraphPad). Striolar surface, HC density and number of
789 Type I and type II HC density in each region of the maculae were plotted individually.
790 Their distribution was framed by 25-75% whisker boxes where exterior lines show the
791 minimum and the maximum, the middle line represents the median, and + represents the
792 mean. Difference of data distribution was tested using Mann-Whitney U (non-parametric,
793 unpaired t-test) for striolar surface and HC density, and 2-way ANOVA with Sidak's
794 multiple comparison for type I and type II HCs.
795
796 **Mouse hair cell and afferent electrophysiology (Figures 2-4, Figure 8)**
797 We followed procedures described in (Gonzalez-Garrido et al., 2021) to prepare and
798 record from HCs and calyceal afferent terminals in semi-intact utricles comprising the
799 sensory epithelium and attached distal vestibular nerve including the vestibular ganglion.
800 Recordings were analyzed for 83 cells from 57 *Gpr156* heterozygotes and 93 cells from
801 73 *Gpr156*-null animals.
802
803 Preparation. Following protocols approved by the University of Chicago Animal Care and
804 Use Committee, mice were deeply anesthetized with gaseous isoflurane and then
805 decapitated to allow dissection of the utricles and attached nerve and ganglion. The
806 preparations were dissected in our *standard bath (external) solution*: cold Leibovitz's-L15
807 medium (L15, Gibco, #41300-021) supplemented with 10 mM HEPES (4-(2-
808 hydroxyethyl)-1-piperazineethanesulfonic acid) (~315 mmol/kg, pH 7.4). The utricles

809 were then treated with L15 containing proteinase XXIV (100 mg/ml, Sigma, St. Louis, MO
810 #P8038) for 11 min at room temperature to facilitate mechanical removal of the otolithic
811 membrane. The epithelium was mounted on a cover slip with glued glass fibers and
812 placed in a recording chamber on a microscope (Zeiss, Axio Examiner A1) equipped with
813 Nomarski and fluorescence optics.
814
815 Recording. For whole-cell recording, pipettes (R6, King Precision Glass) were heat-pulled
816 (PC100, Narishige) and parafilm-wrapped to reduce capacitance. Pipette resistances
817 were 4-5 MΩ for the standard internal and external solutions. Standard internal solution
818 contained (in mM): 135 KCl, 0.1 $CaCl_2$, 3.5 $MgCl_2$, 3 Na_2ATP, 5 creatine phosphate (Na
819 salt), 0.1 Na-cAMP, 0.1 Li-GTP, 5 EGTA, and 10 HEPES, plus ~28 mM KOH to bring pH
820 to 7.3 and osmolality to ~300 mmol/kg. Internal solution was supplemented with
821 sulforhodamine 101 (1 mg/100 ml; Thermo Fisher Scientific) for visualization of recorded
822 hair cells. The bath (external solution) was modified L15 described above and perfused
823 during the experiment.
824
825 We were able to locate LES, striola or MES despite loss of the LPR because anatomical
826 features of the striola are maintained in the otolith organs of *Gpr156* $^{del/del}$ mice (Kindt et
827 al., 2021), and some of these (hair bundle size, spacing of HCs, abundance of complex
828 calyces) are visible in live tissue with Nomarski optics. Usually we aimed for HCs or
829 calyces >50 μm away from zonal boundaries to avoid confusion over zone. In one
830 experimental series, however, we focused on the zonal boundary to see whether afferents
831 respected zonal boundaries in Gpr156-deleted mice.
832
833 To record in whole-cell mode from a specific HC or afferent calyx, we cleaned the cell
834 membrane by the outflow of pipette solution and applied gentle suction to promote giga-
835 seal formation and membrane rupture. Stimulus protocols and data acquisition were
836 implemented by the patch clamp amplifier (model EPC-10, HEKA Elektronik) controlled
837 by Patchmaster software. Data were digitized at sampling intervals of 10 or 20
838 microseconds. Pipette and membrane capacitive currents were nulled and series
839 resistance (R_s) was compensated by 80% on-line with the amplifier's controls. Voltages

840 were corrected offline for the liquid junction potential (–4 mV) and the voltage error due
841 to residual R_s (20% of total R_s, 8.1 ± 0.1, n = 207).
842
843 Mechanical stimulation of mouse hair cells. Hair bundles were deflected with a rigid probe
844 (pulled glass pipette, BF120-60-10, Sutter instrument Company) glued to a piezoelectric
845 bimorph ceramic and brought into contact with the staircase of stereocilia ('back' of the
846 bundle) at ~half-height. Displacement of the probe to driving voltage was calibrated with
847 a CCD camera, yielding a scale factor 330-410 nm/V, depending on the probe. Probe
848 motion recorded with a photodiode (PIN-6D, United Detector Technology) revealed a
849 primary resonance at 1900-2000 Hz. To attenuate this ringing, the voltage input to the
850 bimorph was low-pass filtered (8-pole Bessel filter, Model 900, Frequency Devices) set
851 at 1 kHz, for a step rise time (10-90%) of ~300 μs.
852
853 Mechanotransduction current was recorded in voltage-clamp mode with the holding
854 potential (HP) of –94 mV and –84 mV for type I and type II HCs, respectively. The larger
855 negative potential for type I HCs was chosen to reduce $g_{K,L}$ and so improve the voltage
856 clamp. Responses to three identical displacement step protocols were averaged and low-
857 pass filtered off line (corner frequency, 2 kHz, 8-pole Bessel filter, as above). Step
858 protocols comprised either 20 or 40 displacement steps iterated by 100 nm or 35 nm,
859 respectively, and beginning slightly negative to the resting bundle position. Transduction
860 sensitivity and adaptation was analyzed in 49 HCs with I_{max} > 150 pA (23 HCs from
861 heterozygotes and 26 HCs from null mutants), as described next.
862
863 **Quantification of mouse electrophysiological data**. Analysis of I_{MET} properties is
864 described elsewhere (Songer and Eatock, 2013; Vollrath and Eatock, 2003). Briefly,
865 conductance-displacement [G(X)] activation curves were calculated by dividing I_{MET}
866 (averaged across 2-4 presentations) by the driving force (HP – I_{MET} reversal potential, 0.2
867 mV) (Corns et al., 2014) and plotting G_{MET} against probe displacement (*X*). Probe
868 displacement as a function of driving voltage was calibrated off-line with a photodiode
869 (Songer and Eatock, 2013). G(X) curves were averaged across HCs and fitted with a
870 Boltzmann function (Eq. 1):

871

872 $$G_{MET}(X) = \frac{G_{max} - G_{min}}{1 + e^{(\frac{X_{1/2} - X}{S})}} + G_{min} \quad (1)$$

873

874 where G_{max} and G_{min} are maximum and minimum MET conductance, respectively, $X_{1/2}$ is
875 displacement that evokes half-maximal G_{MET} and S is displacement corresponding to an
876 e-fold rise in G_{MET}. We used the Boltzmann fits to calculate operating range (OR):
877 displacement range corresponding to 10 - 90% of the response range, $G_{max} - G_{min}$.
878

879 We characterized transducer adaptation for responses at $X_{1/2}$, shown previously to reveal
880 both fast and slow components of adaptation in mouse utricular hair cells (Vollrath and
881 Eatock 2003). To reduce noise, current responses were averaged (*n* usually 3) and low-
882 pass filtered at 1.5 kHz. Fast and slow adaptation components were estimated from
883 double-exponential fits of the first 300 ms of the step response (Eq. 2). Deviation of those
884 fits at the onset response signaled a very fast transducer adaptation component, which
885 was separately estimated with a single-exponential fit of the first 1.5 ms of the response
886 (Eq. 3).
887

888 $$I(t) = A_{\mathrm{f}} e^{-\frac{t}{\tau_f}} + A_{\mathrm{s}} e^{-\frac{t}{\tau_s}} + I_{\mathrm{ss}} \quad (2)$$

889

890 $$I(t) = A_{\mathrm{vf}} e^{-\frac{t}{\tau_{vf}}} + I_{\mathrm{ss}} \quad (3)$$

891

892 Here τ_{vf}, τ_f and τ_s are the very short (1 ms or less), short (from 1 to 10 ms) and long (>10
893 ms) time constants, respectively; A_{vf}, A_f and A_s are the amplitudes of the corresponding
894 exponential terms; and I_{SS} is the steady-state current. All HCs had a very fast or fast
895 component or both; some lacked a slow component that was detectable in the 400-ms
896 step.
897

898 We calculated extent of adaptation (% decay) at $X_{1/2}$ as follows (Eq. 4):
899

900 $$Extent\ of\ adaptation = \left(\frac{I_{\ peak} - I_{ss}}{I_{peak} - I_0}\right) \times 100 \quad (4)$$

901

902 where I_0, I_{peak}, and I_{SS} are pre-step, steady-state, and peak currents, respectively.

903

904 In mouse utricular HCs, the dominant voltage-gated currents are carried by outwardly
905 rectifying K_V channels (Martin et al., 2023). By the end of the first postnatal week, these
906 currents provide distinctive electrophysiological signatures in type I and type II HCs, which
907 include more negatively activating K^+ currents and more negative resting potentials for
908 type I HCs (Rusch and Eatock, 1996; Rusch et al., 1998). To characterize the voltage
909 dependence of the currents, we applied families of iterated test voltage steps (400 ms
910 duration) from holding potentials of –74 mV (type I HCs) and –64 mV (type II HCs). The
911 different holding potentials reflect the difference in resting potentials of the two HC types.
912 Steady-state voltage dependence was measured by constructing conductance-voltage
913 [G(V)] relations from tail currents, measured 1 ms after the 400-ms test voltage steps, at
914 a common membrane voltage of –39 mV (chosen to reduce contamination of tail currents
915 by HCN currents). Tail current was converted to "tail conductance" by dividing by driving
916 force ($V_m - V_{rev}$), where V_{rev} is approximated by the K^+ equilibrium potential (–84 mV in
917 our solutions). Tail conductance was plotted against the iterated test step voltage and fit
918 with the Boltzmann function:

919

920 $$G(V) = \frac{G_{max} - G_{min}}{1 + e^{(V_{1/2} - V)/S)}} + G_{min} \ (5)$$

921

922 where $V_{1/2}$ is the voltage of half-maximal activation and S is the voltage change over
923 which G changes e-fold at voltages negative to $V_{1/2}$. Voltage was corrected for voltage
924 errors caused by residual R_S and for the liquid junction potential by subtracting 4 mV.
925 Input resistance (R_{in}) was estimated from current clamp data as the slope of a linear
926 regression of the V_m(I) relation for small currents around resting potential.

927

928 **Imaging of afferent terminal arbors in mouse utricle (Figure 6)**

929 To investigate whether afferent receptive fields (terminal arbors) were disrupted by the
930 lack of bundle reversal in the lateral extrastriola (LES), we recorded in whole-cell mode
931 from calyces near the LES-striolar border. To label the terminal arbors for imaging, we
932 included Alexa Fluor 594 (#A10438 Thermo Fisher Scientific) instead of sulforhodamine
933 in the pipette solution (50 micromolar). After whole-cell recording was achieved, we
934 waited 20 min as the fluorescent pipette solution diffused into the calyx and throughout
935 the terminal arbor, then removed the pipette and fixed the utricular epithelium with 4%
936 paraformaldehyde for 10 min at room temperature (~22°). Fixed utricles were immersed
937 in blocking buffer (PBS with 4% normal donkey serum and 0.2% triton) then treated with
938 primary antibodies diluted with blocking buffer overnight at 4°C. Primary antibodies were:
939 mouse monoclonal anti-βII spectrin (1:500; BD Transduction, #612562) , to label hair
940 bundles and show the location of the kinocilium by absence of label; rabbit polyclonal
941 anti-calbindin (1:250; Invitrogen, #711443) to label the striola and juxtastriola (Leonard
942 and Kevetter, 2002). Specimens were then washed extensively and incubated with
943 secondary antibodies conjugated with fluorescent proteins (donkey anti-mouse or rabbit
944 IgG (H + L) antibody, ThermoFisher Scientific) for 1 hr at 4°C. Stained specimens were
945 mounted whole in mounting medium (Vector Laboratories, #H-1500), imaged with
946 spinning-disc confocal microscopy (Marianas SDC 3i), and analyzed with Adobe
947 Photoshop 2021 and FluoRender (ver. 2.26.3).
948
949 **Measurement of excitability from mouse utricular afferents (Figure 8)**
950 To document excitability of afferents in the LES, we recorded from calyces in whole-cell
951 current clamp mode, injected current steps and noted the thresholds for spiking and the
952 firing patterns. Most LES afferents are dimorphic, forming both calyces and boutons on
953 type I and II HCs, respectively. We rejected calyces with resting potentials less negative
954 than –50 mV. We evoked spikes with current steps to determine if afferents had step-
955 evoked firing patterns consistent with expected zonal patterns of spiking regularity in
956 mammalian vestibular epithelia (Goldberg et al., 1990; Iwasaki et al., 2008; Kalluri et al.,
957 2010). Families of 500-ms current steps were applied from zero-current potential,
958 beginning at –200 pA and incremented by 50 pA. Threshold current (I_{thresh}) was taken as
959 the minimum current (±50 pA) required to evoke any spikes.

960

961 We classified neuronal firing patterns according to the number of spikes evoked by a 400-
962 ms step at $I_m = 3\times I_{thresh}$ (Ono et al., 2020): a pattern of 1-2 spikes at step onset was
963 considered 'transient'; if more spikes were evoked, the pattern was 'sustained'. These
964 patterns have been associated with the mechanisms that give rise to well-known
965 differences in the regularity of firing across zones. The transient step-evoked pattern is
966 associated with striolar, irregular afferents and the sustained step-evoked pattern with
967 extrastriolar, regular afferents. The difference in step-evoked firing patterns is attributed
968 to zonal differences in expression of K_V channels that influence spike regularity (Iwasaki
969 et al., 2008; Kalluri et al., 2010) and, more importantly, encoding strategy of afferent fibers
970 (Jamali et al., 2019).

971

972 **Data analysis and statistics – mouse electrophysiology (Figures 2-4, Figure 8)**

973 Data analysis, statistical tests, curve fitting and graphing were done with OriginPro (2022;
974 OriginLab, Northampton, MA), Clampfit (Molecular Probes) and Matlab (Mathworks,
975 Natick, MA). For samples that had homogeneous variance, significance was tested with
976 either a two-tailed t-test or a one-way ANOVA with post-hoc Tukey test. When samples
977 had unequal variance, we used either Welch's t-test or Kruskal-Wallis ANOVA with post-
978 hoc Mann-Whitney U test. For significant differences ($p < 0.05$), we calculated effect size
979 with Hedge's g equation. For non-significant (NS) differences, we calculated statistical
980 power *post hoc* (OriginPro 2022) and these values are entered in tables along with p-
981 values.

982

983 **Quantification of vestibular reflexes in mice (Figures 11-12)**

984 We tested the angular vestibulo-ocular reflex (aVOR), the optokinetic reflex (OKR), and
985 the otolith vestibulo-ocular reflex (off-vertical axis rotation, OVAR). Specifically, aVOR
986 tests semicircular canal function, whereas OVAR tests otolith function. For completeness
987 we also tested each animal's OKR as a control of the integrity of visuo-motor function.

988

989 **aVOR and OKR.** Surgical techniques and experimental setup have been previously
990 described (Beraneck and Cullen, 2007). Eye movement data were collected using an

991 infrared video system (ETL-200, ISCAN system). The rotational velocity of the turntable
992 (head velocity) was measured using a MEMS sensor (MPU-9250, SparkFun Electronics).
993 Eye movements during the OKR were evoked by sinusoidal rotations of a visual surround
994 (vertical black and white stripes, visual angle width of 5°) placed around the turntable at
995 frequencies 0.2, 0.4, 0.8, 1, 2, and 3 Hz with peak velocities of ±16°/s. To record VOR
996 responses, the turntable was rotated at sinusoidal frequencies 0.2, 0.4, 0.8, 1, 2, and 3
997 Hz with peak velocities of ±16°/s in both light and dark. In the light condition, the visual
998 surround remained stationary, whereas, in the dark condition, both the visual surround
999 and turntable rotated in phase and the surroundings was made dark. Head and eye
1000 movement signals were low-passed filtered at 125 Hz and sampled at 1 kHz. Eye position
1001 data were differentiated to obtain velocity traces. Cycles of data with quick phases were
1002 excluded from the analysis. Least-square optimization determined the VOR and OKR
1003 gains, and phases plotted as mean ± standard error of the mean (SEM) against all
1004 frequencies for all mice.
1005
1006 **OVAR.** Techniques employed for measurement of eye movements during OVAR in alert
1007 mice were described elsewhere (Beraneck et al., 2012). Briefly, recordings made after
1008 fixating mice on a rotating platform, which was tilted 17° with respect to the ground. The
1009 platform speed was increased from 0 to 50°/s in 500 ms and maintained its constant
1010 velocity for 72 s (10 complete rounds) before being stopped. Eye movements were
1011 measured using the same Infrared video system (ETL-200, ISCAN system) used for
1012 angular VOR and OKR recordings. Quick phases were identified as previously described
1013 and excluded from subsequent analysis. We then estimated the time constant of the
1014 OVAR slow-phase eye velocity response decay, as well as the amplitude and phase of
1015 its sinusoidal modulation using a linear regression approach.
1016
1017 **Mouse swimming assessment**
1018 A large container (26.25 × 16.25 × 14.38′) was filled with water (24–26°C) at the height
1019 of at least 15 cm. The mouse was placed into the water and observed for up to 1 min. Its
1020 performance was rated using the following scale (Hardisty-Hughes et al., 2010):
1021 0 = swims, body elongated, and tail propels in flagella-like motion.

1022 1 = immobile floating.
1023 2 = underwater tumbling.
1024 In a time-to-rescue trial, if an animal exhibited distressed swimming (underwater
1025 tumbling) before 60 seconds, the animal was rescued and time of rescue was marked. If
1026 not, the trial was marked as lasting 60 seconds.
1027
1028 **Mouse balance beam assessment**
1029 A 6-mm-wide and 40-cm-long beam was used for balance beam testing. The mice
1030 traversed 40 cm to a dark box. Walking speed was measured by recording the time the
1031 mouse took to reach the goal box from the opposite end of the beam. Mice were scored
1032 "time out" if they failed to reach the endpoint in 2 min.
1033
1034 **Air Righting, Tailing Hanging, and Contact Inhibition of Righting Tests**
1035 *Air Righting Test*
1036 The mouse was picked up by the tail and lowered into a container (size of container?) so
1037 that all four feet touched the bottom. The container was quickly inverted at a height of
1038 30–40 cm so mouse fell supine onto a foam cushion below. How the mouse landed was
1039 observed and rated as below (Rabbath et al., 2001):
1040 0 = the animal lands on its feet (normal).
1041 1 = the animal lands on its side (mild deficit).
1042 2 = the animal lands on its back (severe deficit).
1043
1044 *Tail Hanging Test*
1045 The animal was picked up by the tail and lowered to an even surface, and its posture
1046 rated using the following scale (Rabbath et al., 2001):
1047 0 = straight body posture with extension of forelimbs toward the earth (normal).
1048 1 = slightly bending the body ventrally (intermediate response).
1049 2 = persistently bending the body (severe response).
1050
1051 *Contact Inhibition of Righting Test*
1052 The mouse was picked up by the tail and lowered into a small container so that all four

1053 feet were in contact with the bottom, then the top of the container closed in contact with
1054 the mouse's back. The container was then quickly inverted so that the mouse became
1055 supine while the surface remains in contact with the soles of the mouse's feet. The
1056 mouse's reflex was rated using the following scale (Rabbath et al., 2001):
1057 0 = animal rights successfully (normal).
1058 1 = partial righting (intermediate response).
1059 2 = complete loss of righting (severe response).
1060
1061 **Quantification of Tremor during Resting Head Movement (Supplemental fig. 2)**
1062 Mice were placed in a cylinder (9 cm diameter and 21.5 cm height) that limited their
1063 motion, so mice maintained their steady posture. Head movements in six dimensions
1064 were recorded for 2 minutes using a miniature head motion sensor (MPU-9250,
1065 SparkFun Electronics, Niwot, CO, United States) affixed on the top of the skull, which
1066 comprises a three-dimensional (3D) accelerometer (measures linear acceleration;
1067 fore/aft, lateral, and vertical) and 3D gyroscope (measures angular velocity: roll, pitch,
1068 and yaw). Data was acquired at 200 Hz using windows-based CoolTerm software. We
1069 then computed the power spectral densities (pwelch function, MATLAB, MathWorks)
1070 using Welch's averaged periodogram with nfft = 4,096 and a Bartlett window (4,096 ms
1071 duration) for all six dimensions of movement.
1072
1073 **Data analysis and statistics – mouse behavior (Figures 11-12)**
1074 Data are reported as the mean ± SEM. Nonparametric Mann-Whitney U-test was
1075 performed to test significance for time to traverse (balance beam) and time to rescue
1076 (swimming) between two groups. Two-way repeated-measures ANOVA followed by
1077 Bonferroni post hoc comparison tests was used for the VOR data across frequencies. For
1078 power spectra analysis we used an independent sample permutation test to test
1079 significant differences between the two groups. Prism 9 (GraphPad) or MATLAB was
1080 used for statistical analyses. The same independent sample permutation test was also
1081 used to test significance for bias and gain of OVAR responses.
1082
1083 **Zebrafish strains and husbandry**

1084 Zebrafish (*Danio rerio*) were grown at 30 °C using a 14 hr light, 10 hr dark cycle. Larvae
1085 were raised in E3 embryo medium (5 mM NaCl, 0.17 mM KCl, 0.33 mM $CaCl_2$, and
1086 0.33 mM $MgSO_4$, pH 7.2). Larvae were examined at 5-6 days post fertilization (dpf). The
1087 following previously established mutant and transgenic zebrafish strains were used in this
1088 study: *gpr156*^{idc15}, *emx2*^{idc5} (Jiang et al., 2017; Kindt et al., 2021),
1089 *Tg(myo6b:memGCaMP6s*^{idc1} (Kindt et al., 2021). For comparisons, *emx2* mutants were
1090 compared to wild-type or *emx2*$^{+/-}$ animals. *Gpr156* mutants were compared to *gpr156*$^{+/-}$
1091 animals. Zebrafish work was performed at the National Institute of Health (NIH) and
1092 approved by the Animal Use Committee at the NIH under animal study protocol #1362-
1093 13.
1094
1095 **Zebrafish immunofluorescence and imaging (Figures 5, Figures 9-10)**
1096 Immunohistochemistry was performed on whole larvae at 5 dpf. Whole larvae were fixed
1097 with 4% paraformaldehyde in PBS at 4°C for 3.5 hr. For pre- and post-synaptic labeling
1098 all wash, block and antibody solutions were prepared with 0.1% Tween in PBS (PBST).
1099 For Emx2 labeling performed on sparse afferent labeling (see below) all wash, block and
1100 antibody solutions were prepared with PBS + 1% DMSO, 0.5% Triton-X100, 0.1% Tween-
1101 20 (PBDTT). After fixation, larvae were washed 4 × 5 min in PBST or PBDTT. For synaptic
1102 labeling, larvae were permeabilized with Acetone. For this permeabilization larvae were
1103 washed for 5 min with H_2O. The H_2O was removed and replaced with ice-cold acetone
1104 and placed at −20°C for 5 min, followed by a 5 min H_2O wash. The larvae were then
1105 washed for 4 × 5 min in PBST. For all immunostains larvae were blocked overnight at 4°C
1106 in blocking solution (2% goat serum, 1% bovine serum albumin, 2% fish skin gelatin in
1107 PBST or PBDTT). Larvae were then incubated in primary antibodies in antibody solution
1108 (1% bovine serum albumin in PBST or PBDTT) overnight, nutating at 4°C. The next day,
1109 the larvae were washed for 4 × 5 min in PBST or PBDTT to remove the primary antibodies.
1110 Secondary antibodies in antibody solution were added and larvae were incubated for 2
1111 hrs at room temperature, with minimal exposure to light. Secondary antibodies were
1112 washed out with PBST or PBDTT for 4 × 5 min. Larvae were mounted on glass slides
1113 with Prolong Gold (ThermoFisher Scientific) using No. 1.5 coverslips. Primary antibodies
1114 used were:

1115 Rabbit anti-Myo7a (Proteus 25-6790; 1:1000)
1116 Mouse anti-Ribeye b (IgG2a) (Sheets et al., 2011)
1117 Mouse anti-pan-MAGUK (IgG1) (Millipore MABN7; 1:500)
1118 Mouse anti-Myo7a (DSHB 138-1; 1:500)
1119 Rabbit anti-Emx2 (Trans Genic KO609; 1:250).
1120 The following secondaries were used at 1:1000 for synaptic labeling: goat anti-rabbit
1121 Alexa 488, goat anti-mouse IgG2a Alexa 546, goat anti-mouse IgG1 Alexa 647, along
1122 with Alexa 488 Phalloidin (Thermofischer; #A-11008, #A-21133, #A-21240, #A12379).
1123 For Emx2 co-labeling the following secondaries were used at 1:1000: goat anti-mouse
1124 Alexa 488, and goat ant-rabbit Alexa 647, along with Alexa 488 Phalloidin (Thermofischer;
1125 #A12379, #A28175, #A27040).
1126 Fixed samples were imaged on an inverted Zeiss LSM 780 laser-scanning confocal
1127 microscope with an Airyscan attachment (Carl Zeiss AG, Oberkochen, Germany) using
1128 an 63 × 1.4 NA oil objective lens. Airyscan z-stacks were acquired every 0.18 µm. The
1129 Airyscan Z-stacks were processed with Zen Black software v2.1 using 2D filter setting of
1130 6.0. Experiments were imaged with the same acquisition settings to maintain consistency
1131 between comparisons. Processed imaged were further processed using Fiji.
1132
1133 **Zebrafish immunostain quantification (Figure 5, Figures 9-10)**
1134 Images were processed in ImageJ. Researcher was not blinded to genotype. Hair bundle
1135 orientation was scored relative to the midline of the muscle somites. HC number per
1136 neuromast were quantified based on Myo7a labeling and presence of a paired/complete
1137 synapse. For quantification of Emx2 labeling, HCs were scored as Emx2 positive if they
1138 labeled with both Emx2 and Myo7a. To quality as a ribbon or presynapse, the following
1139 minimum size filters were applied to images: Ribeye b: 0.025 μm^2, MAGUK: 0.04 μm^2. A
1140 complete synapse was comprised of both a Ribeye b and MAGUK puntca. An unpaired
1141 presynapse consisted of only a Ribeye b puntca, while an unpaired postsynapse
1142 consisted of only a MAGUK puncta. In each neuromast all HCs (~15 HC per neuromast)
1143 were examined for our quantifications.
1144
1145 **Zebrafish functional calcium imaging in hair bundles (Figure 5)**

1146 GCaMP6s-based calcium imaging in zebrafish hair bundles has been previously
1147 described (Lukasz and Kindt, 2018). Briefly, individual 5-6 dpf larvae were first
1148 anesthetized with tricaine (0.03% Ethyl 3-aminobenzoate methanesulfonate salt,
1149 SigmaAldrich). To restrain larvae, they were then pinned to a Sylgard-filled recording
1150 chamber. To suppress the movement, alpha-bungarotoxin (125 μM, Tocris) was injected
1151 into the heart. Larvae were then rinsed and immersed in extracellular imaging solution (in
1152 mM: 140 NaCl, 2 KCl, 2 $CaCl_2$, 1 $MgCl_2$ and 10 HEPES, pH 7.3, OSM 310 +/- 10) without
1153 tricaine. A fluid jet was used to mechanically stimulate the apical bundles of HCs of the
1154 A-P neuromasts of the primary posterior lateral-line. To stimulate the two orientations of
1155 HCs (A>P and P>A) a 500 ms 'push' was delivered. Larvae were rotated 180° to deliver
1156 a comparable 'push' stimulus to both the A>P and P>A HCs.
1157
1158 To image calcium-dependent mechanosensitive responses in apical hair bundles, a
1159 Bruker Swept-field confocal system was used. The Bruker Swept-field confocal system
1160 was equipped with a Rolera EM-C2 CCD camera (QImaging) and a Nikon CFI Fluor
1161 60× 1.0 NA water immersion objective. Images were acquired in 5 planes along the Z-
1162 axis at 0.5 μm intervals (hair bundles) at a 50 Hz frame rate (10 Hz volume rate). The 5
1163 plane Z-stacks were projected into one plane for image processing and quantification.
1164 The method to create spatial ΔF heatmaps has been described (Lukasz and Kindt, 2018).
1165 For GCaMP6s measurements, a circular ROI with a ~1.5 μm (hair bundles) diameter was
1166 placed on the center of each individual bundle. The mean intensity ($\Delta F/F_0$) within each
1167 ROI was quantified. F_0 represents the GCaMP6s intensity prior to stimulation. We
1168 examined the GCaMP6s signal in each hair bundle to determine its orientation. The
1169 GCaMP6s responses for each neuromast were averaged to quantify the magnitude of the
1170 A>P and P>A responses.
1171
1172 **Zebrafish sparse labeling of single afferents in the lateral-line (Figure 9)**
1173 To visualize the innervation pattern of single afferent neurons, a *neuroD1:tdTomato*
1174 plasmid was injected into zebrafish embryos at the 1-cell stage. This plasmid consists of
1175 a 5kb minimal promoter, *neurod1*, that drives tdTomato expression in lateral-line afferents
1176 (Ji et al., 2018). This plasmid was pressure at a concentration of 30 ng/μl. At 3 dpf larvae

1177 were anesthetized with 0.03% ethyl 3-aminobenzoate methanesulfonate (Tricaine), to
1178 screen for tdTomato expression. Larvae were screened for mosaic expression of
1179 tdTomato expression in the lateral-line afferents using a Zeiss SteREO Discovery V20
1180 microscope (Carl Zeiss) with an X-Cite 120 external fluorescent light source (EXFO
1181 Photonic Solutions Inc). After selecting larvae with tdTomato expression, larvae were
1182 prepared for immunostaining at 5 dpf, and imaged as outlined above.

1183

1184 **Zebrafish data analysis and statistics**

1185 Statistical analyses and data plots were performed with Prism 9 (Graphpad, San Diego,
1186 CA). Values of data with error bars on graphs and in text are expressed as mean ± SEM
1187 unless indicated otherwise. All experiments were performed on a minimum of 3 animals,
1188 6 neuromasts (primary posterior lateral-line neuromasts with A-P orientations: L1-L5). For
1189 5-6 dpf larvae, each neuromast represents analysis from 12 to 20 HCs and 41–68
1190 synapses. All replicates are biological. No animals or samples were excluded from our
1191 analyses unless control experiments failed–in these cases all samples were excluded.
1192 No randomization or blinding was used for our animal studies. Where appropriate, data
1193 was confirmed for normality using a D'Agostino-Pearson normality test. Statistical
1194 significance between conditions was determined by an unpaired *t* -test.

1195

1196

1197 **REFERENCES**

1198

1199 **Beraneck, M., Bojados, M., Le Seac'h, A., Jamon, M. and Vidal, P. P.** (2012). Ontogeny of
1200 mouse vestibulo-ocular reflex following genetic or environmental alteration of gravity
1201 sensing. *PLoS One* **7**, e40414.
1202 **Chitnis, A. B., Nogare, D. D. and Matsuda, M.** (2012). Building the posterior lateral line system
1203 in zebrafish. *Dev Neurobiol* **72**, 234-255.
1204 **Chou, S. W., Chen, Z., Zhu, S., Davis, R. W., Hu, J., Liu, L., Fernando, C. A., Kindig, K., Brown, W.**
1205 **C., Stepanyan, R., et al.** (2017). A molecular basis for water motion detection by the
1206 mechanosensory lateral line of zebrafish. *Nature communications* **8**, 2234.
1207 **Corns, L. F., Johnson, S. L., Kros, C. J. and Marcotti, W.** (2014). Calcium entry into stereocilia
1208 drives adaptation of the mechanoelectrical transducer current of mammalian cochlear
1209 hair cells. *PNAS* **111**, 14918-14923.
1210 **Cullen, K. E.** (2019). Vestibular processing during natural self-motion: implications for
1211 perception and action. *Nat Rev Neurosci* **20**, 346-363.
1212 **Daigle, T. L., Madisen, L., Hage, T. A., Valley, M. T., Knoblich, U., Larsen, R. S., Takeno, M. M.,**
1213 **Huang, L., Gu, H., Larsen, R., et al.** (2018). A Suite of Transgenic Driver and Reporter
1214 Mouse Lines with Enhanced Brain-Cell-Type Targeting and Functionality. *Cell* **174**, 465-
1215 480 e422.
1216 **Deans, M. R.** (2013). A balance of form and function: planar polarity and development of the
1217 vestibular maculae. *Seminars in cell & developmental biology* **24**, 490-498.
1218 **Deans, M. R., Antic, D., Suyama, K., Scott, M. P., Axelrod, J. D. and Goodrich, L. V.** (2007).
1219 Asymmetric distribution of prickle-like 2 reveals an early underlying polarization of
1220 vestibular sensory epithelia in the inner ear. *J Neurosci* **27**, 3139-3147.
1221 **Denman-Johnson, K. and Forge, A.** (1999). Establishment of hair bundle polarity and
1222 orientation in the developing vestibular system of the mouse. *J Neurocytol* **28**, 821-835.
1223 **Eatock, R. A. and Songer, J. E.** (2011). Vestibular hair cells and afferents: two channels for head
1224 motion signals. *Annu Rev Neurosci* **34**, 501-534.
1225 **Fernandez, C., Goldberg, J. M. and Abend, W. K.** (1972). Response to static tilts of peripheral
1226 neurons innervating otolith organs of the squirrel monkey. *J Neurophysiol* **35**, 978-987.
1227 **Fernandez, C., Goldberg, J. M. and Baird, R. A.** (1990). The vestibular nerve of the chinchilla. III.
1228 Peripheral innervation patterns in the utricular macula. *J Neurophysiol* **63**, 767-780.
1229 **Flock, A.** (1964). Structure of the Macula Utriculi with Special Reference to Directional Interplay
1230 of Sensory Responses as Revealed by Morphological Polarization. *J Cell Biol* **22**, 413-431.
1231 **Goldberg, J. M.** (1991). The vestibular end organs: morphological and physiological diversity of
1232 afferents. *Current opinion in neurobiology* **1**, 229-235.
1233 **----** (2000). Afferent diversity and the organization of central vestibular pathways. *Exp Brain Res*
1234 **130**, 277-297.
1235 **Goldberg, J. M., Desmadryl, G., Baird, R. A. and Fernandez, C.** (1990). The vestibular nerve of
1236 the chinchilla. V. Relation between afferent discharge properties and peripheral
1237 innervation patterns in the utricular macula. *J Neurophysiol* **63**, 791-804.

1238 **Gonzalez-Garrido, A., Pujol, R., Lopez-Ramirez, O., Finkbeiner, C., Eatock, R. A. and Stone, J. S.**
1239 (2021). The Differentiation Status of Hair Cells That Regenerate Naturally in the
1240 Vestibular Inner Ear of the Adult Mouse. *J Neurosci* **41**, 7779-7796.
1241 **Holley, M., Rhodes, C., Kneebone, A., Herde, M. K., Fleming, M. and Steel, K. P.** (2010). Emx2
1242 and early hair cell development in the mouse inner ear. *Dev Biol* **340**, 547-556.
1243 **Iwasaki, S., Chihara, Y., Komuta, Y., Ito, K. and Sahara, Y.** (2008). Low-voltage-activated
1244 potassium channels underlie the regulation of intrinsic firing properties of rat vestibular
1245 ganglion cells. *J Neurophysiol* **100**, 2192-2204.
1246 **Jacobo, A., Dasgupta, A., Erzberger, A., Siletti, K. and Hudspeth, A. J.** (2019). Notch-Mediated
1247 Determination of Hair-Bundle Polarity in Mechanosensory Hair Cells of the Zebrafish
1248 Lateral Line. *Current biology : CB* **29**, 3579-3587 e3577.
1249 **Jamali, M., Carriot, J., Chacron, M. J. and Cullen, K. E.** (2019). Coding strategies in the otolith
1250 system differ for translational head motion vs. static orientation relative to gravity. *eLife*
1251 **8**.
1252 **Ji, Y. R., Tona, Y., Wafa, T., Christman, M. E., Tourney, E. D., Jiang, T., Ohta, S., Cheng, H.,**
1253 **Fitzgerald, T., Fritzsch, B., et al.** (2022). Function of bidirectional sensitivity in the otolith
1254 organs established by transcription factor Emx2. *Nature communications* **13**, 6330.
1255 **Ji, Y. R., Warrier, S., Jiang, T., Wu, D. K. and Kindt, K. S.** (2018). Directional selectivity of
1256 afferent neurons in zebrafish neuromasts is regulated by Emx2 in presynaptic hair cells.
1257 *eLife* **7**.
1258 **Jiang, T., Kindt, K. and Wu, D. K.** (2017). Transcription factor Emx2 controls stereociliary bundle
1259 orientation of sensory hair cells. *eLife* **6**.
1260 **Jones, C., Qian, D., Kim, S. M., Li, S., Ren, D., Knapp, L., Sprinzak, D., Avraham, K. B.,**
1261 **Matsuzaki, F., Chi, F., et al.** (2014). Ankrd6 is a mammalian functional homolog of
1262 Drosophila planar cell polarity gene diego and regulates coordinated cellular orientation
1263 in the mouse inner ear. *Dev Biol* **395**, 62-72.
1264 **Kalluri, R., Xue, J. and Eatock, R. A.** (2010). Ion channels set spike timing regularity of
1265 mammalian vestibular afferent neurons. *J Neurophysiol* **104**, 2034-2051.
1266 **Kindig, K., Stepanyan, R., Kindt, K. S. and McDermott, B. M., Jr.** (2023). Asymmetric
1267 mechanotransduction by hair cells of the zebrafish lateral line. *Current biology : CB* **33**,
1268 1295-1307 e1293.
1269 **Kindt, K. S., Akturk, A., Jarysta, A., Day, M., Beirl, A., Flonard, M. and Tarchini, B.** (2021).
1270 EMX2-GPR156-Galphai reverses hair cell orientation in mechanosensory epithelia.
1271 *Nature communications* **12**, 2861.
1272 **Kozak, E. L., Palit, S., Miranda-Rodriguez, J. R., Janjic, A., Bottcher, A., Lickert, H., Enard, W.,**
1273 **Theis, F. J. and Lopez-Schier, H.** (2020). Epithelial Planar Bipolarity Emerges from Notch-
1274 Mediated Asymmetric Inhibition of Emx2. *Current biology : CB* **30**, 1142-1151 e1146.
1275 **Lein, E. S., Hawrylycz, M. J., Ao, N., Ayres, M., Bensinger, A., Bernard, A., Boe, A. F., Boguski,**
1276 **M. S., Brockway, K. S., Byrnes, E. J., et al.** (2007). Genome-wide atlas of gene expression
1277 in the adult mouse brain. *Nature* **445**, 168-176.
1278 **Leonard, R. B. and Kevetter, G. A.** (2002). Molecular probes of the vestibular nerve. I.
1279 Peripheral termination patterns of calretinin, calbindin and peripherin containing fibers.
1280 *Brain Res* **928**, 8-17.

1281 **Li, A., Xue, J. and Peterson, E. H.** (2008). Architecture of the mouse utricle: macular
1282 organization and hair bundle heights. *J Neurophysiol* **99**, 718-733.
1283 **Lindeman, H. H.** (1969). Regional differences in structure of the vestibular sensory regions. *The*
1284 *Journal of laryngology and otology* **83**, 1-17.
1285 **Lopez-Schier, H., Starr, C. J., Kappler, J. A., Kollmar, R. and Hudspeth, A. J.** (2004). Directional
1286 cell migration establishes the axes of planar polarity in the posterior lateral-line organ of
1287 the zebrafish. *Dev Cell* **7**, 401-412.
1288 **Lozano-Ortega, M., Valera, G., Xiao, Y., Faucherre, A. and Lopez-Schier, H.** (2018). Hair cell
1289 identity establishes labeled lines of directional mechanosensation. *PLoS biology* **16**,
1290 e2004404.
1291 **Maklad, A., Kamel, S., Wong, E. and Fritzsch, B.** (2010). Development and organization of
1292 polarity-specific segregation of primary vestibular afferent fibers in mice. *Cell and tissue*
1293 *research* **340**, 303-321.
1294 **Martin, H. R., Lysakowski, A. and Eatock, R. A.** (2023). The potassium channel subunit K(V)1.8
1295 (Kcna10) is essential for the distinctive outwardly rectifying conductances of type I and II
1296 vestibular hair cells. *bioRxiv*.
1297 **McInturff, S., Burns, J. C. and Kelley, M. W.** (2018). Characterization of spatial and temporal
1298 development of Type I and Type II hair cells in the mouse utricle using new cell-type-
1299 specific markers. *Biol Open* **7**.
1300 **Mirkovic, I., Pylawka, S. and Hudspeth, A. J.** (2012). Rearrangements between differentiating
1301 hair cells coordinate planar polarity and the establishment of mirror symmetry in
1302 lateral-line neuromasts. *Biol Open* **1**, 498-505.
1303 **Ono, K., Keller, J., Lopez Ramirez, O., Gonzalez Garrido, A., Zobeiri, O. A., Chang, H. H. V.,**
1304 **Vijayakumar, S., Ayiotis, A., Duester, G., Della Santina, C. C., et al.** (2020). Retinoic acid
1305 degradation shapes zonal development of vestibular organs and sensitivity to transient
1306 linear accelerations. *Nature communications* **11**, 63.
1307 **Rusch, A. and Eatock, R. A.** (1996). A delayed rectifier conductance in type I hair cells of the
1308 mouse utricle. *J Neurophysiol* **76**, 995-1004.
1309 **Rusch, A., Lysakowski, A. and Eatock, R. A.** (1998). Postnatal development of type I and type II
1310 hair cells in the mouse utricle: acquisition of voltage-gated conductances and
1311 differentiated morphology. *J Neurosci* **18**, 7487-7501.
1312 **Sheets, L., Trapani, J. G., Mo, W., Obholzer, N. and Nicolson, T.** (2011). Ribeye is required for
1313 presynaptic Ca(V)1.3a channel localization and afferent innervation of sensory hair cells.
1314 *Development* **138**, 1309-1319.
1315 **Simmons, D. D., Tong, B., Schrader, A. D. and Hornak, A. J.** (2010). Oncomodulin identifies
1316 different hair cell types in the mammalian inner ear. *J Comp Neurol* **518**, 3785-3802.
1317 **Songer, J. E. and Eatock, R. A.** (2013). Tuning and timing in mammalian type I hair cells and
1318 calyceal synapses. *J Neurosci* **33**, 3706-3724.
1319 **Tarchini, B.** (2021). A Reversal in Hair Cell Orientation Organizes Both the Auditory and
1320 Vestibular Organs. *Front Neurosci* **15**, 695914.
1321 **Ventura, C. M. and Kalluri, R.** (2019). Enhanced Activation of HCN Channels Reduces Excitability
1322 and Spike-Timing Regularity in Maturing Vestibular Afferent Neurons. *J Neurosci* **39**,
1323 2860-2876.

1324 **Vollrath, M. A. and Eatock, R. A.** (2003). Time course and extent of mechanotransducer
1325 adaptation in mouse utricular hair cells: comparison with frog saccular hair cells. *J*
1326 *Neurophysiol* **90**, 2676-2689.
1327 **Xue, J. and Peterson, E. H.** (2006). Hair bundle heights in the utricle: differences between
1328 macular locations and hair cell types. *J Neurophysiol* **95**, 171-186.
1329 **Zhou, X., Wang, L., Hasegawa, H., Amin, P., Han, B. X., Kaneko, S., He, Y. and Wang, F.** (2010).
1330 Deletion of PIK3C3/Vps34 in sensory neurons causes rapid neurodegeneration by
1331 disrupting the endosomal but not the autophagic pathway. *PNAS* **107**, 9424-9429.
1332

1333

1334

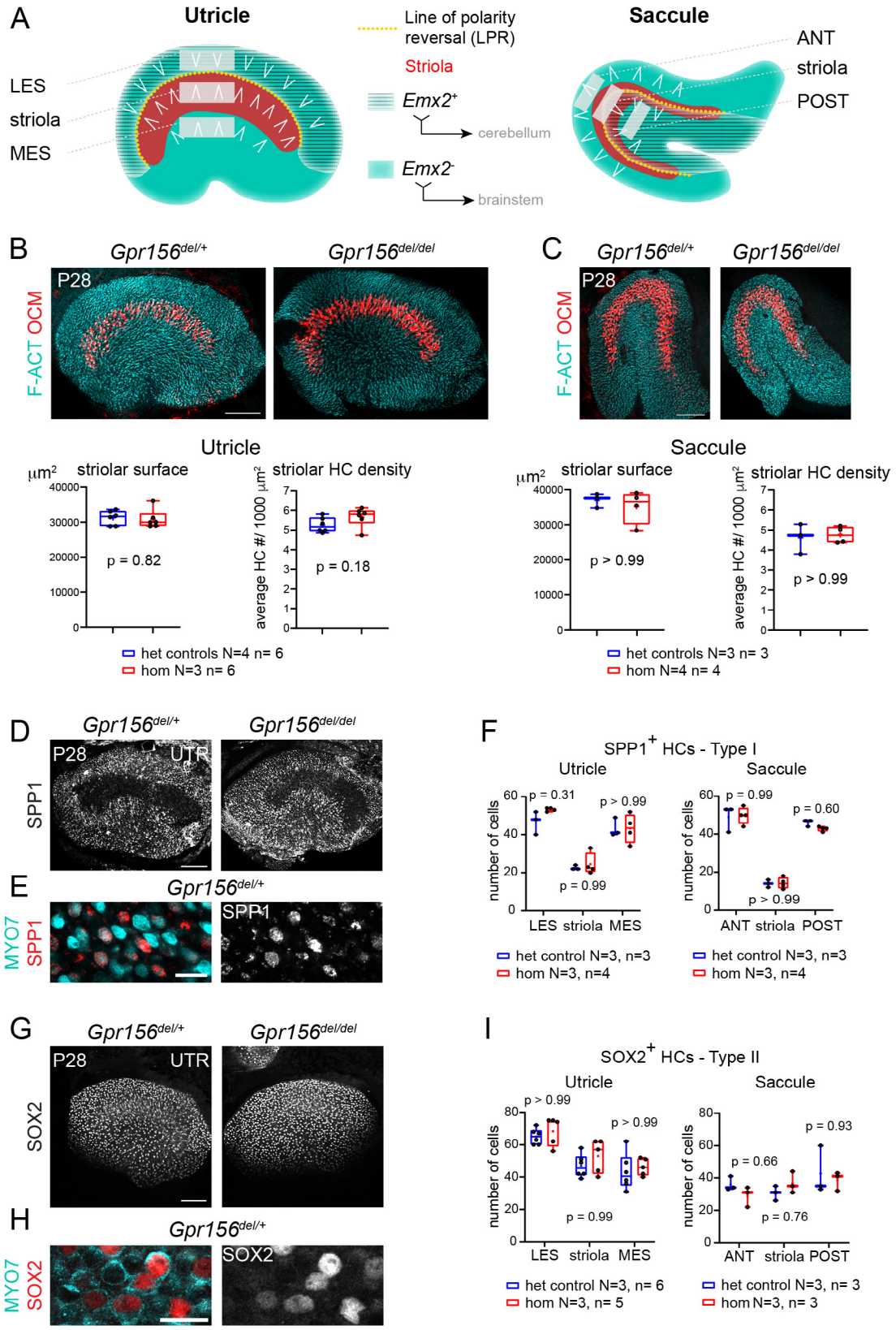
A
Utricle
Saccule
Line of polarity reversal (LPR)
Striola
Emx2+
cerebellum
Emx2-
brainstem
LES
striola
MES
ANT
striola
POST
B
Gpr156del/+
Gpr156del/del
P28
F-ACT OCM
C
Utricle
Saccule
μm2 striolar surface
average HC #/ 1000 μm2 striolar HC density
p = 0.82
p = 0.18
p > 0.99
p > 0.99
het controls N=4 n= 6
hom N=3 n= 6
het controls N=3 n= 3
hom N=4 n= 4
D
SPP1
UTR
E
MYO7
SPP1
F
SPP1+ HCs - Type I
number of cells
p = 0.31
p > 0.99
p = 0.99
p = 0.99
p > 0.99
p = 0.60
p > 0.99
LES striola MES
ANT striola POST
het control N=3, n=3
hom N=3, n=4
G
SOX2
H
MYO7
SOX2
I
SOX2+ HCs - Type II
p > 0.99
p > 0.99
p = 0.99
p = 0.66
p = 0.93
p = 0.76
LES striola MES
ANT striola POST
het control N=3, n= 6
hom N=3, n= 5
het control N=3, n= 3
hom N=3, n= 3

1335

1336 **Figure 1. Normal striola and hair cell type organization in *Gpr156* mutants. A**)
1337 Diagrams showing general macular organization and the regions analyzed in **B-I** (LES,
1338 MES: lateral and medial extrastriola, respectively; ANT: anterior, POST: posterior). Each
1339 region is 130x50 μm in the utricle and 150x40 μm in the saccule. White chevrons indicate
1340 HC orientation. **B-C**) P28 utricles (**B**) and saccules (**C**) immunolabeled with oncomodulin
1341 (OCM) to reveal the striolar region and phalloidin to reveal F-actin (F-ACT)-rich hair
1342 bundles. Graphs report striolar surface area and striolar HC density based on OCM
1343 labeling and show no change in mutants compared to heterozygote littermate controls.
1344 All points are graphed along with 25-75% boxplots (external bars: minimum and maximum,
1345 internal bar: median, cross: mean). Mann-Whitney U test. **D-F**) P28 maculae
1346 immunolabeled with SPP1 to reveal type I HCs. Low magnification of the utricle (**D**), high
1347 magnification view showing SPP1 at the utricle HC neck (**E**), and quantification per region
1348 in utricle and saccule (**F**). **G-I**) P28 maculae immunolabeled with SOX2 to reveal type II
1349 HCs. Low magnification of the utricle (**G**), high magnification view showing SOX2 in the
1350 utricle HC nucleus (**H**), and quantification per region in utricle and saccule (**I**). **F**, **I:** 2-way
1351 ANOVA with Sidak's multiple comparisons. N, n: number of animals and HCs,
1352 respectively. UTR, utricle. Scale bars: 100 μm (**B**-**C**, **D**, **G**), 10 μm (**E**, **H**).
1353

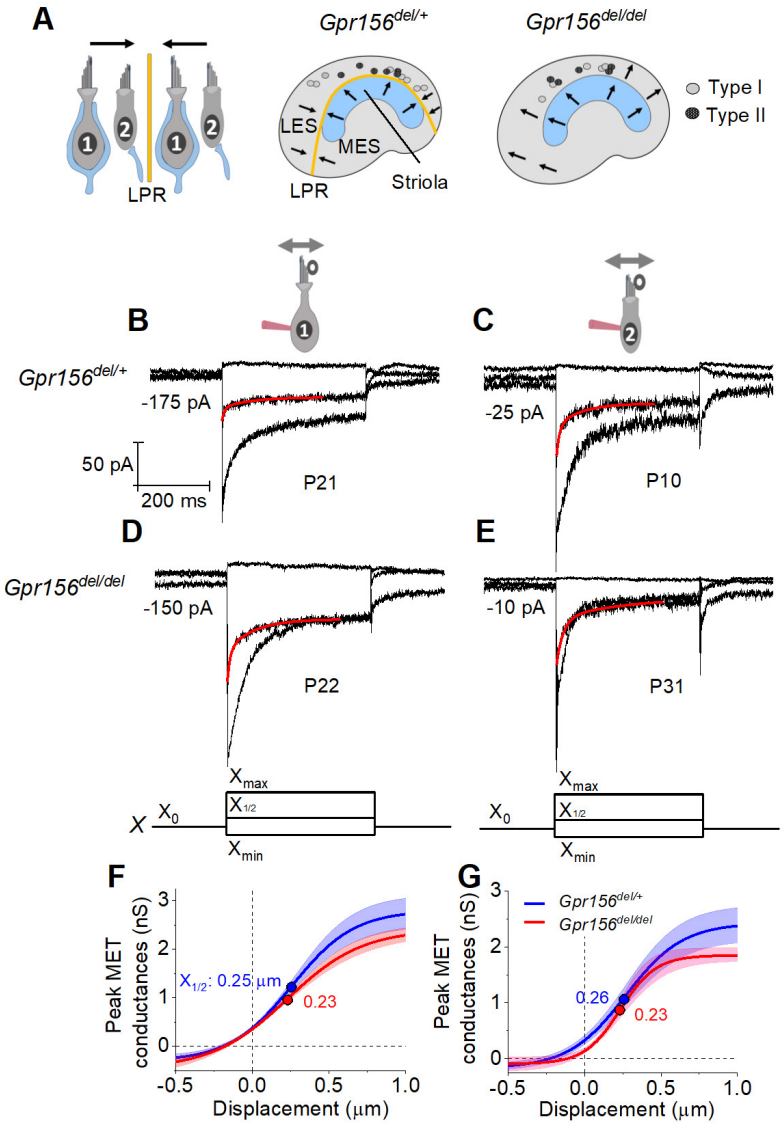

1354

1355

1356 **Figure 2. No effects of *Gpr156* deletion on mechanosensitivity were detected in LES**
1357 **hair cells. A**) *Left,* Schematic showing hair cell types with normal reversed bundle polarity
1358 at the LPR. *Arrows*, Directions of hair bundle motion that produce a depolarizing receptor
1359 potential. *Right,* Maps of recordings from LES zone, lateral to the LPR in heterozygotes,
1360 and similar location in null mutants, but without bundle reversal (arrows). **B-E**) Exemplar
1361 I_{MET} recordings from voltage-clamped LES HCs of different type (I vs. II, columns) and
1362 genotype (het vs. null, rows), and ranging in age from P10 to P31. XY scales for all 4 are
1363 in **D**. Each panel shows I_{MET} current (average of 3 traces) evoked by 3 of many iterated
1364 bundle displacements (bottom of **D,E**): negatively and positively saturating stimuli (X_{min},

1365 X_{max}) plus a step to ~ $X_{1/2}$ (midpoint) of the operating range. *Red traces*, fits of current
1366 decay for step to $X_{1/2}$ with Eq. 2 or 3 (Methods). Voltage was clamped with the indicated
1367 holding currents at –94 mV (type I) and –84 mV (type II). **F,G**) *G(X*) relations from type I
1368 (**F**) and type II (**G**) HCs. G, was peak MET conductance taken at the onset of each of 20
1369 or 40 displacement steps (*X*), iterated by 100 nm or 35 nm, respectively, and averaged
1370 across 3 repeated stimulus families. *Mean ± SEM; n = 5-8 cells.* Fitted *G(X)* parameters
1371 are statistically similar for *Gpr156*$^{del/+}$ and *Gpr156*$^{del/del}$ HCs (see Table 2). *Filled circles,*
1372 $X_{1/2}$ values from fits. X_{max}: 1.1 to 1.3 micrometers. X_{min}; –0.2 to –0.45 micrometers.
1373

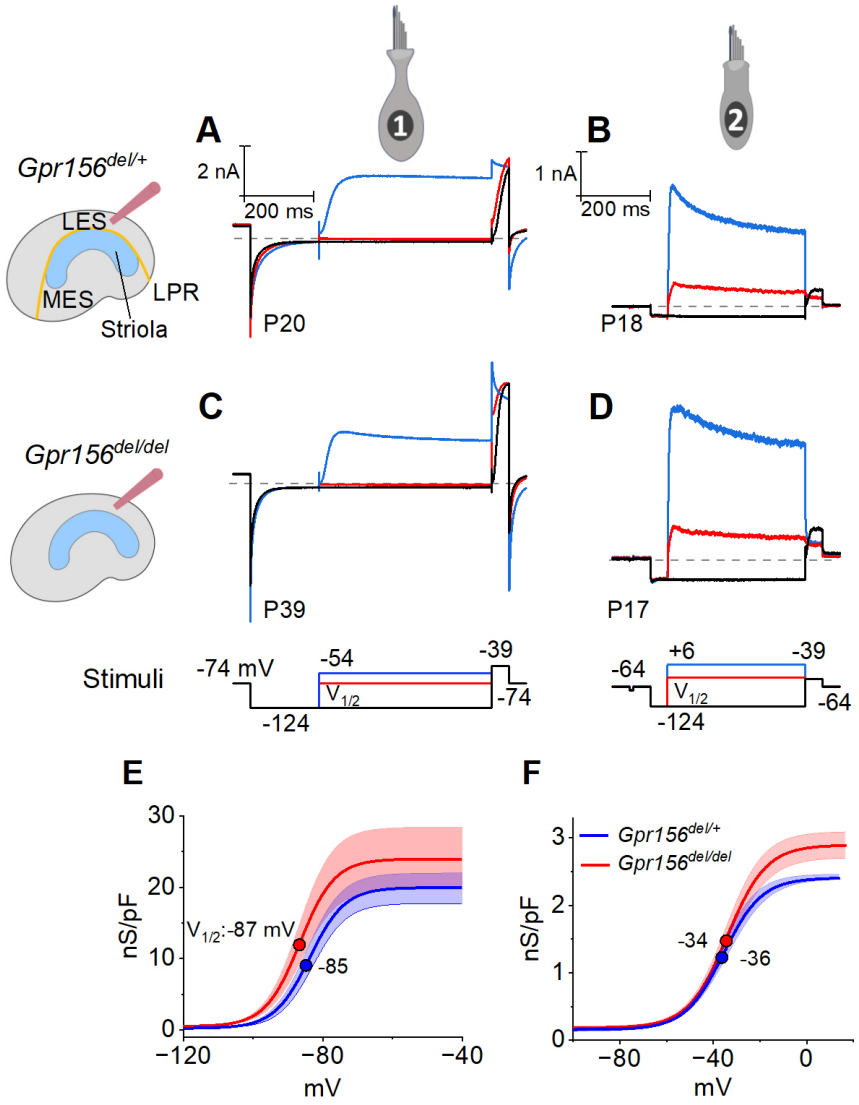

Figure 3. No effects of *Gpr156* deletion on basolateral voltage-dependent conductances were detected in LES HCs. A-D) Exemplar voltage-dependent currents from lateral extrastriolar (LES) type I (a, c) and type II (b, d) HCs of *Gpr156*$^{del/+}$ (**A**, **B**) and *Gpr156*$^{del/del}$ (**C**, **D**) utricles. There are significant differences between HC types, but these differences are seen in both *Gpr156*$^{del/+}$ (**A,B**) and *Gpr156*$^{del/del}$ utricles (**C,D**). A pre-pulse from holding potential to –124 mV shows the usual type I-type II difference in K^+ conductances at or near resting potential: the prepulse deactivates $g_{K,L}$ in type I cells (**A,C**), and activates a small inwardly rectifying current in type II cells (**B,D**). Following the pre-pulse, test steps were iterated in 5-mV increments from –124 mV to –54 mV (type I)

1385 or from –124 mV to +6 mV (type II), activating currents with very different time course and
1386 voltage dependence. **E,F**) G(V) relations measured from tail currents at the end of the
1387 iterated voltage steps show that $g_{K,L}$ activated positive to –114 mV (**E**) while type II
1388 delayed rectifying currents activated positive to –64 mV (**F**).

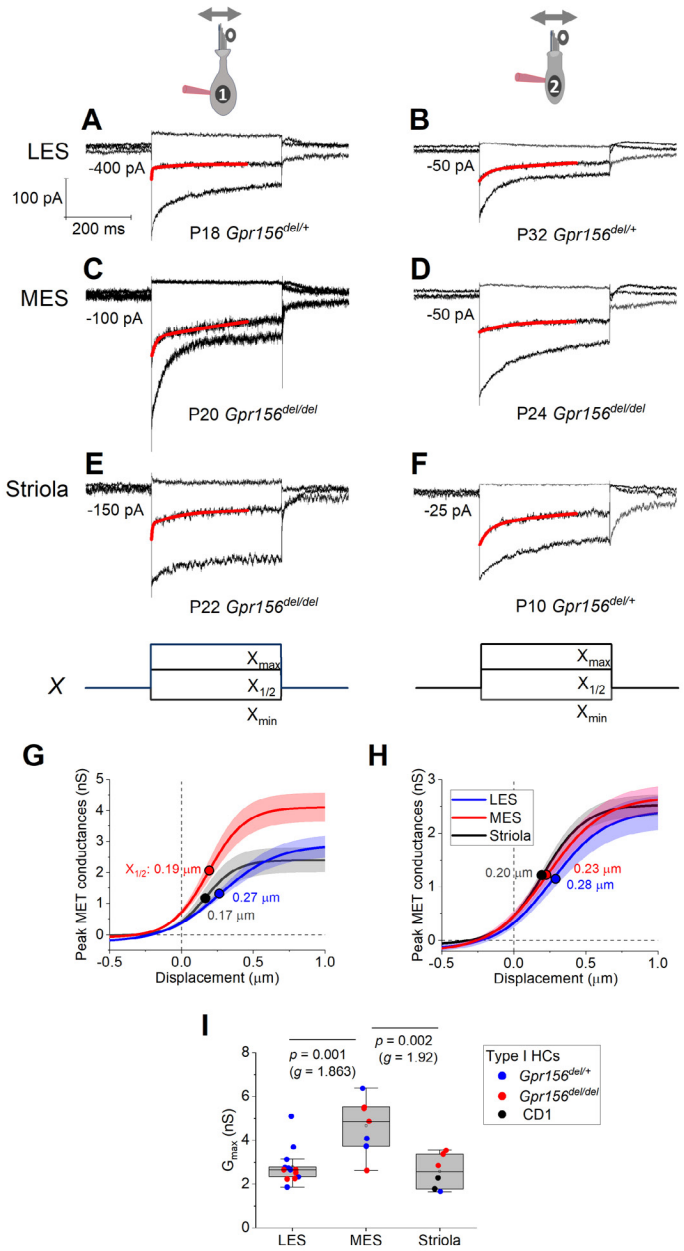

Figure 4. Displacement sensitivity and time course of step-evoked transduction currents in each zone were not strongly affected by Gpr156 deletion. A-F) Exemplar I_{MET} recordings from voltage-clamped HCs of different genotype, HC type (columns), and epithelial zone (rows). I_{MET} current families (averages of 3) evoked by 3 of many iterated bundle displacements (**E,F**, bottom): negatively and positively saturating stimuli plus the step closest to the midpoint ($X_{1/2}$) of the G(X) relation. X_{max}: 1.08 to 1.32 µm. X_{min}: –0.2 to –0.45 µm. *Red traces*, fits of current decay with Eq. 2 or 3 (Methods). Holding potentials,

1397 –94 mV (type I) and –84 mV (type II). **G-H**) Averaged peak (onset) $G_{MET}(X)$ relations for
1398 type I (**G**) and type II (**H**) HCs. Data from 5-9 HCs of each type were fitted with the
1399 Boltzmann functions, which were averaged to produce mean curves shown (± SEM). $X_{1/2}$
1400 values (filled circles) are given. **I**) Mean maximum G_{MET} of type I HCs was larger in MES
1401 than in LES or striola, but there was not a significant effect of genotype. *Black circles*, 2
1402 striolar type I HCs from CD1 mice.
1403

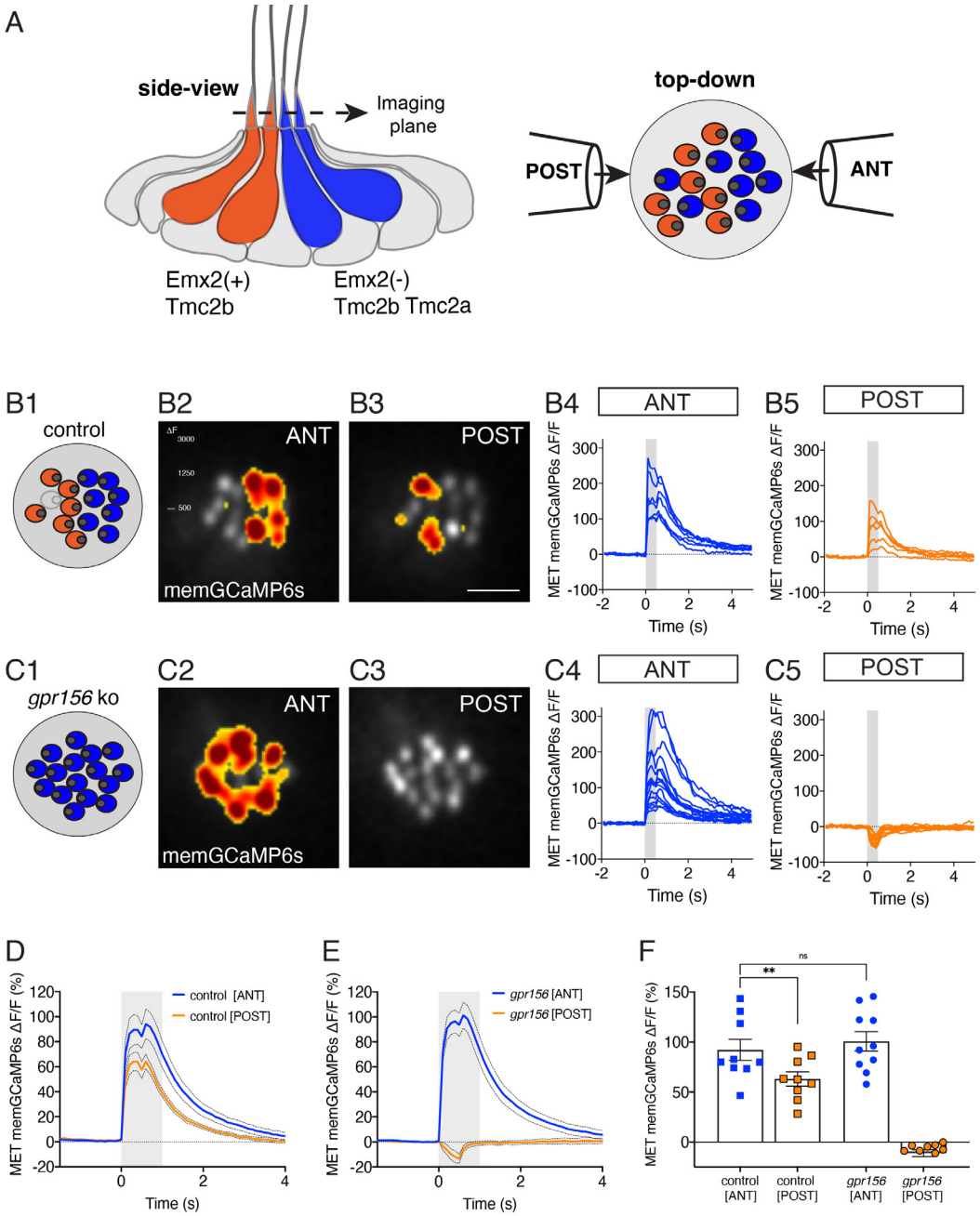

Figure 5. Gpr156 impacted the mechanosensitive properties of lateral-line HCs. A) Schematic on the left shows a lateral-line neuromast from the side. HCs that detect anterior and posterior flow are color coded in blue and orange respectively. Posterior HCs do not express Emx2 and rely primarily on the MET channel subunits Tmc2a and Tmc2b. In contrast, anterior HCs express Emx2 and rely primary on Tmc2b for mechanosensation. Schematic on the right shows a plane taken through the apical hair bundle plane, viewed top-down. The directional sensitivity of each HC is dictated by the location of the

1412 kinocilium, which is indicated by the circle on the side of each hair bundle. This apical
1413 plane is one used to monitor mechanosensitive-calcium signals in lateral-line hair bundles.
1414 The pipettes on each side of the hair bundles show the direction of flow delivered to
1415 stimulate the two populations of HCs. **B1**-**B5**) Representative example of evoked-
1416 mechanosensitive calcium signals in hair bundles of a control neuromast during a 500-
1417 ms ANT (**B2**) or a 500-ms POST (**B3**) directed stimulus. Spatial patterns of GCaMP6s
1418 signals during stimulation (**B2**-**B3**) are colorized according to the ∆F heat map and
1419 superimposed onto a baseline GCaMP6s image. In **B1**, the colored circles indicate the
1420 respective hair bundle orientation observed from calcium imaging (ANT, orange; POST,
1421 blue; no response, gray). ROIs were placed on each hair bundle to generate the ∆F/F
1422 GCaMP6s traces from individual ANT (**B4**) and POST (**B5**) responding hair bundles. **C1**-
1423 **C5**) Representative example of evoked-mechanosensitive calcium signals in hair bundles
1424 of a *gpr156* mutant neuromast during a 500-ms ANT (**C2**) or a 500-ms POST (**C3**)
1425 directed stimulus. Spatial patterns of GCaMP6s signals during stimulation (**C2**-**C3**) are
1426 colorized according to the ∆F heat map in **B2** and superimposed onto a baseline
1427 GCaMP6s image. In **C1**, the colored circles indicate the respective hair bundle orientation
1428 observed from calcium imaging (POST, blue). ROIs were placed on all hair bundle to
1429 generate the ∆F/F GCaMP6s traces from individual hair bundles during ANT (**C4**) and
1430 POST (**C5**) stimuli. **D**-**F)** Quantification of the average increase in GCaMP6s per
1431 neuromast for ANT and POST hair bundles. Traces in **D** and **E** show the average
1432 GCaMP6s response per neuromast in ANT and POST hair-bundle populations (mean ±
1433 SEM is shown in **D**-**E**, n = 9 control and 10 *gpr156* neuromasts). The magnitude of the
1434 GCaMP6s data in **D**-**E** is plotted to compare the average GCaMP6s increase for ANT and
1435 POST hair bundles for each neuromast in **F**. In control neuromasts, the GCaMP6s
1436 increase in the hair bundles ANT cells were larger compared to POST cells. In *gpr156*
1437 mutants the ANT cells were significantly larger than control POST cells, but not different
1438 than control ANT cells. **P = 0.0043 and P = 0.561, paired and unpaired t-test respectively.
1439 Scale bar is 5 µm in **B3**.
1440

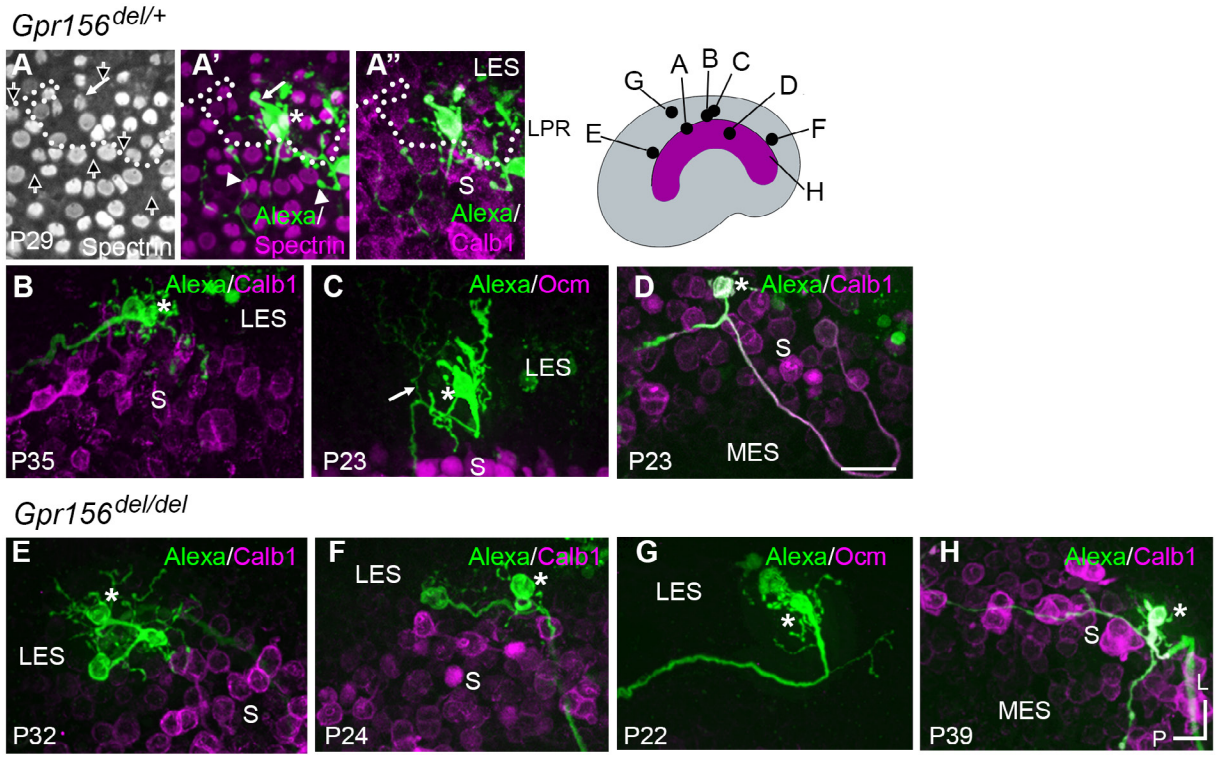

Figure 6. Afferent innervation patterns near the LES/S zone boundary were not substantially disturbed by *Gpr156* deletion. Afferent receptive fields (*green*) were labeled by diffusion of fluorescent dye (AlexaFluor) from whole-cell recording pipettes into calyces (*asterisks*) and throughout the terminal arbor, for (**A**-**D**) *Gpr156*$^{del/+}$ controls and (**E**-**H**) *Gpr156*$^{del/del}$ mutants. Counterstained with anti-calbindin (Calb1) antibody to show the striola (*magenta*). *Top right,* Schematic of the utricle with magenta striola; *black dots*, approximate location of each labelled calyx *shown*. All labeled afferents had a thick, medial-projecting neurite that branched to form up to 2 calyces and many bouton contacts. Anti-βII-spectrin labeling (**A**, **A'**) leaves an unlabeled hole where the kinocilium is, allowing determination of bundle orientation (*black arrows outlined in white, A*) and, in *Gpr156*$^{del/+}$ controls, the LPR (*dotted white line*). **A**) In one control afferent, the receptive field straddled the LPR (**A'**, **A''**), with 1 calyx on a type I HC in the LES (*white arrow*) and some boutons contacting type II HCs, as terminals or en passant, in the calbindin^{+} striola (*white arrowheads*). **B, C**) In all other fills, both control and mutant, the labeled LES arbors innervated only LES HCs. **C,** *arrow*, A thin branch extended from the fiber below the epithelium (Supplemental video). **D**) A receptive field labeled by filling a striolar calyx

1459 included 2 calyces and some bouton endings, all restricted to the calbindin^{+} striola (this
1460 afferent is white because of the merge of AlexaFluor and calbindin stains). **E-G**) Afferent
1461 terminal fields of LES calyces from *Gpr156*$^{del/del}$ utricles largely remained in the calbindin^{-}
1462 region (LES). **H**) A striolar (calbindin^{+}) calyx in a *Gpr156*$^{del/del}$ mouse made multiple
1463 boutons entirely in the calbindin^{+} area (striola). Scale bar: 20 micrometers L, lateral; P,
1464 posterior.
1465

1466

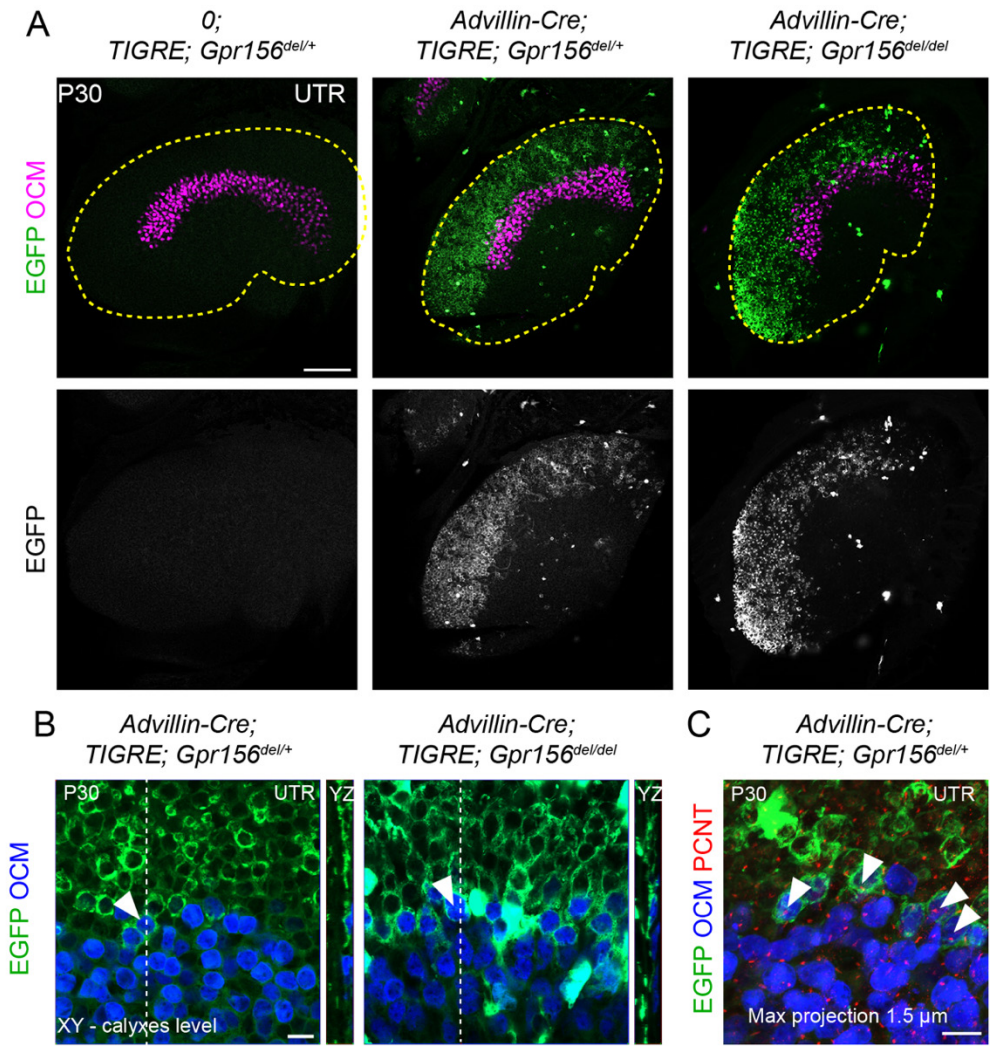

1467

1468 **Figure 7. LES afferent innervation pattern was comparable for *Gpr156*$^{del/+}$ and**
1469 ***Gpr156*$^{del/del}$ utricles. A**) P30 utricles where oncomodulin (OCM) labels striolar HCs and
1470 *Advillin*-positive afferents are labeled by EGFP in *Advillin-Cre; TIGRE; Gpr156* animals.
1471 *Advillin-Cre* neurons specifically innervated lateral HCs and orientation-based
1472 segregation was not altered in *Gpr156*$^{del/del}$ mutants. **B**) Close-up views at the LES-striola
1473 border (XY and YZ views). The vast majority of EGFP-positive HCs were in the the LES
1474 but *Advillin*-positive neurons also innervated OCM^{+} HCs in the lateral striola in both
1475 control and *Gpr156* mutants. **C**) Close-up view where basal bodies are labeled with
1476 pericentrin (PCNT) to reveal HC orientation (arrowheads). Lateral striolar HCs innervated
1477 by *Advillin* neurons were consistently oriented medially, showing that innervation from

1478 *Advillin* neurons strictly segregates with HC orientation, and not with striolar
1479 characteristics (OCM expression). Yellow dotted lines in A mark the outline of the utricle.
1480 Scale bars: 100 μm (A) 10 μm (B-C).
1481

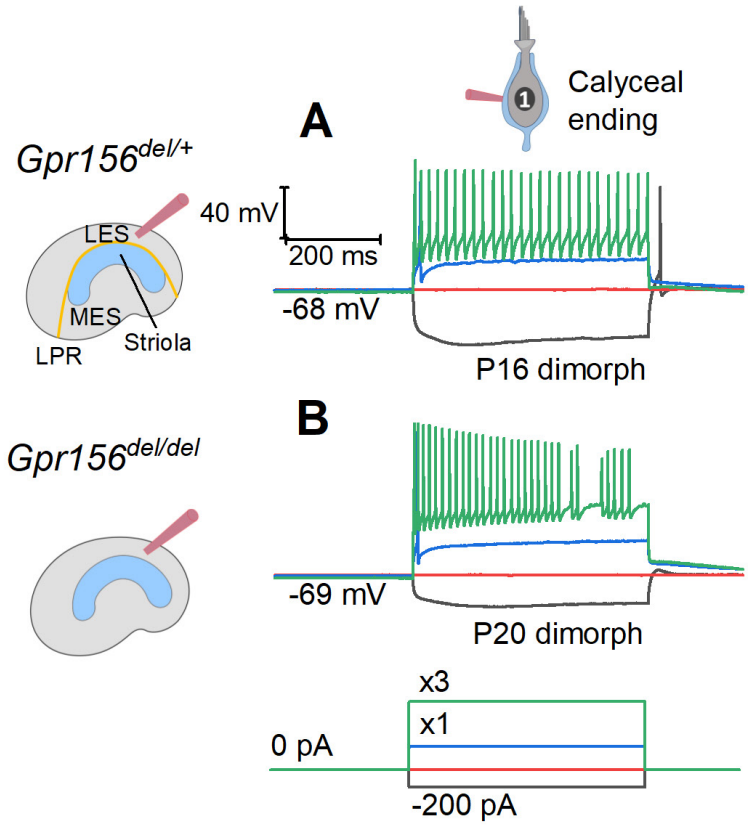

1482

1483

1484 **Figure 8. The excitability of LES afferents was not significantly affected by Gpr156**
1485 **deletion.** Exemplary voltage responses of control (**A**) and null (**B**) afferents to injected
1486 steps of current. We recorded from the large calyceal endings as a way to access these
1487 dimorphic afferents, which, like most LES afferents, made contact with both type I and
1488 type II HCs. For current steps (bottom) at 3 × I_{thresh} (×3, green), both genotypes produced
1489 sustained firing, considered typical of regular afferents innervating LES and MES. Here
1490 I_{thresh} (blue trace) was 100 pA for Gpr156$^{del/+}$ afferent and 250 pA for Gpr156$^{del/del}$ afferent,
1491 but overall there was no significant difference in current threshold with genotype.

1492

1493

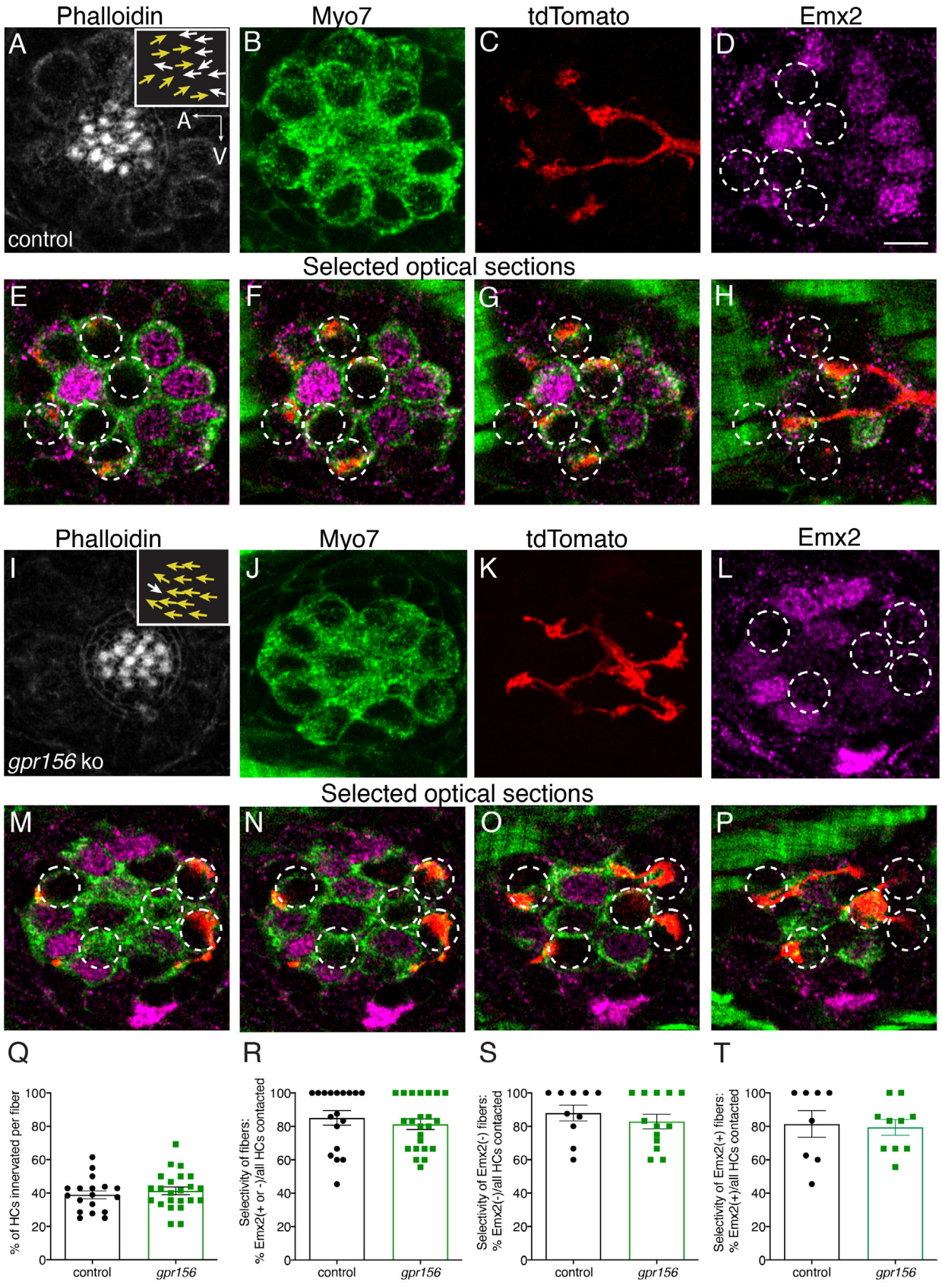
Phalloidin
Myo7
tdTomato
Emx2
A
B
C
D
A
V
control
Selected optical sections
E
F
G
H
Phalloidin
Myo7
tdTomato
Emx2
I
J
K
L
gpr156 ko
Selected optical sections
M
N
O
P
Q
R
S
T
% of HCs innervated per fiber
Selectivity of fibers: % Emx2(+ or -)/all HCs contacted
Selectivity of Emx2(-) fibers: % Emx2(-)/all HCs contacted
Selectivity of Emx2(+) fibers: % Emx2(+)/all HCs contacted
0
20
40
60
80
100
control
gpr156

1494

1495 **Figure 9. Gpr156 was not required for lateral-line afferents to select Emx2^{+} or Emx2^{-}**
1496 **hair cells. A-H**) Images of a control neuromast innervated by a single afferent fiber that
1497 contacts Emx2(-) cells at 5 dpf. **A**) Phalloidin label reveals 16 hair bundles (8 A>P and 8
1498 P>A hair bundles). Z-stack projections show all HCs labeled with Myo7a (**B**) a single
1499 afferent fiber expressing tdTomato (**C)** and Emx2(+ and -) HCs (**D**). **E**-**H**) Selected optical
1500 sections of (**B**–**D**) highlight the single afferent contacting individual Emx2(-) HCs. **I-P**)
1501 Images of a *gpr156* mutant neuromast innervated by a single afferent fiber that contacts
1502 Emx2(-) cells. (**I**) Phalloidin label revealed 14 hair bundles (13 A>P and 1 P>A hair
1503 bundles). Z-stack projections show all HCs labeled with Myo7a (**J**) a single afferent fiber
1504 expressing tdTomato (**K**) and Emx2(+ and -) HCs (**L**). **M-O**) Selected optical sections of
1505 (**J**–**L**) highlight a single afferent in a *gpr156* mutants contacting individual Emx2(-) HCs.
1506 **Q**) In both controls and *gpr156* mutants, each afferent fiber contacted the same number
1507 of HCs per neuromast. **R**) The overall selectivity of afferent fiber for Emx2(+ or -) HCs
1508 were similarly high in *gpr156* mutant and controls. **S**-**T**) The selectivity of afferent fibers
1509 for Emx2(+) or Emx2(-) HCs was similarly high in both *gpr156* mutants and controls.
1510 Arrows in **A** and **I** indicate the orientation of the hair bundles in each example. SEM is
1511 shown in Q-T. An unpaired *t*-test was used for comparisons. Scale bar = 5 μm.
1512

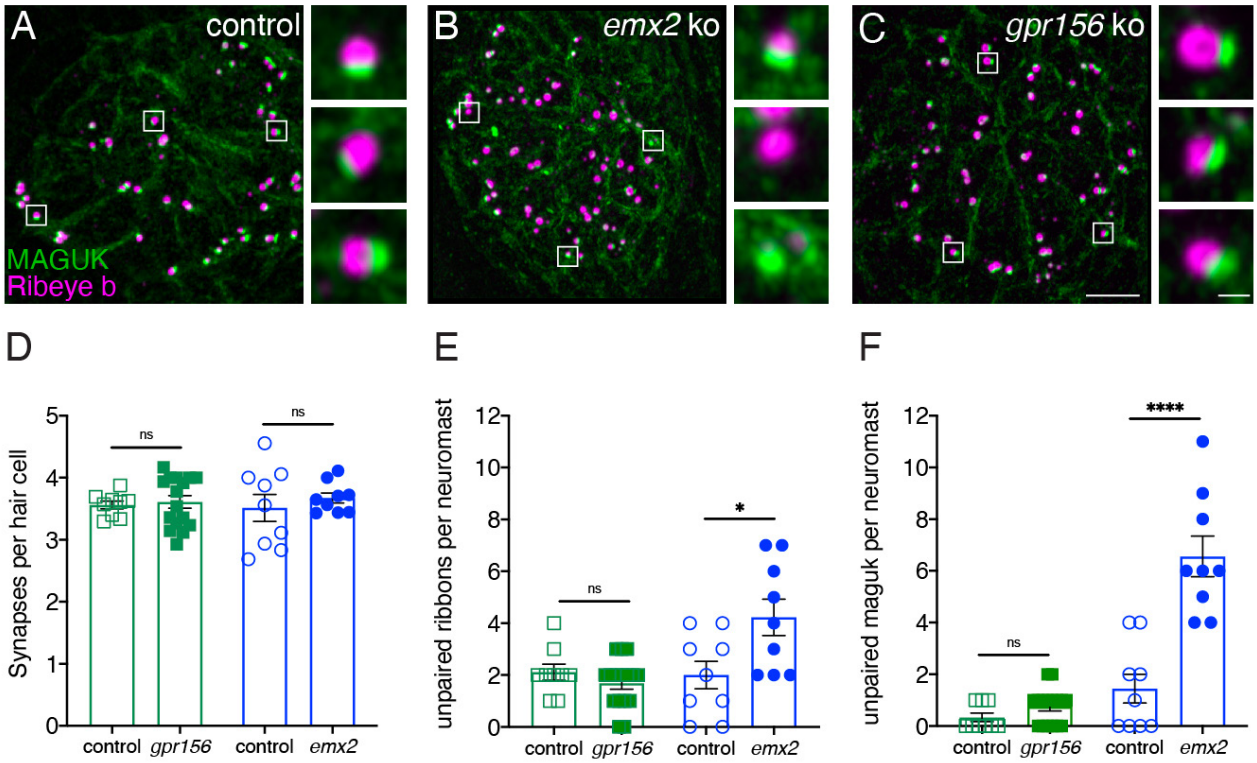

Figure 10. Grp156 was not required for pairing of pre- and post-synapses in lateral-line hair cells. A-C) Images neuromasts immunolabeled with Maguk and Ribeye b to stain HC post- and pre-synapses, respectively at 5 dpf. **A**) Example of an immunostain of a control neuromast showing 3 complete synapses to the right. **B**) Image of an *emx2* mutant neuromast that shows complete synapses, as well as unpaired pre- and postsynapses, shown to the right. **C**) Image of a *gpr156* mutant neuromast, with complete synapses shown to the right. **D**) Quantification revealed the same number of complete synapses per HC in *emx2* and *gpr156* mutants compared to controls. **E-F**) In *gpr156* mutants, quantification revealed there is no difference in the number of unpaired pre- or post-synapses per neuromast compared to controls. In *emx2* mutants, there were significantly more pre- or post-synapses per neuromast compared to controls. SEM is shown in **D-F**. Scale bar = 5 µm. Unpaired t-test were used to make comparisons. *$p < 0.05$, ****$p < 0.0001$.

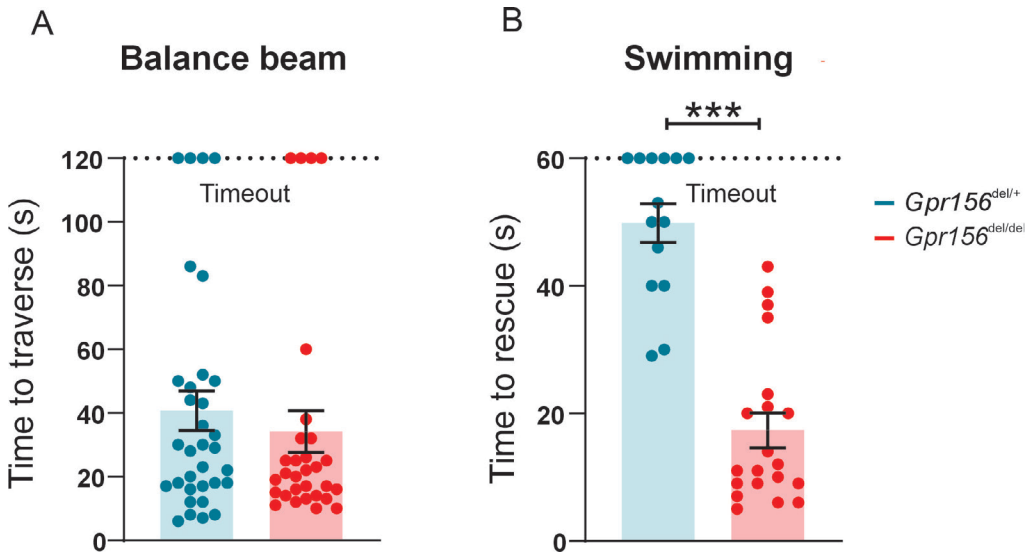

Figure 11. *Gpr156* mutant mice failed to swim and maintain their balance in water. **A**) Time taken to traverse the balance beam for control and *Gpr156*$^{del/del}$ mice. N is 33 and 30 for control (green) and *Gpr156*$^{del/del}$ (red) mice respectively. **B**) Time taken to rescue an animal immediately after the animal exhibited underwater tumbling. N is 14 and 20 for control (green) and *Gpr156*$^{del/del}$ (red) mice respectively. ***P<0.001.

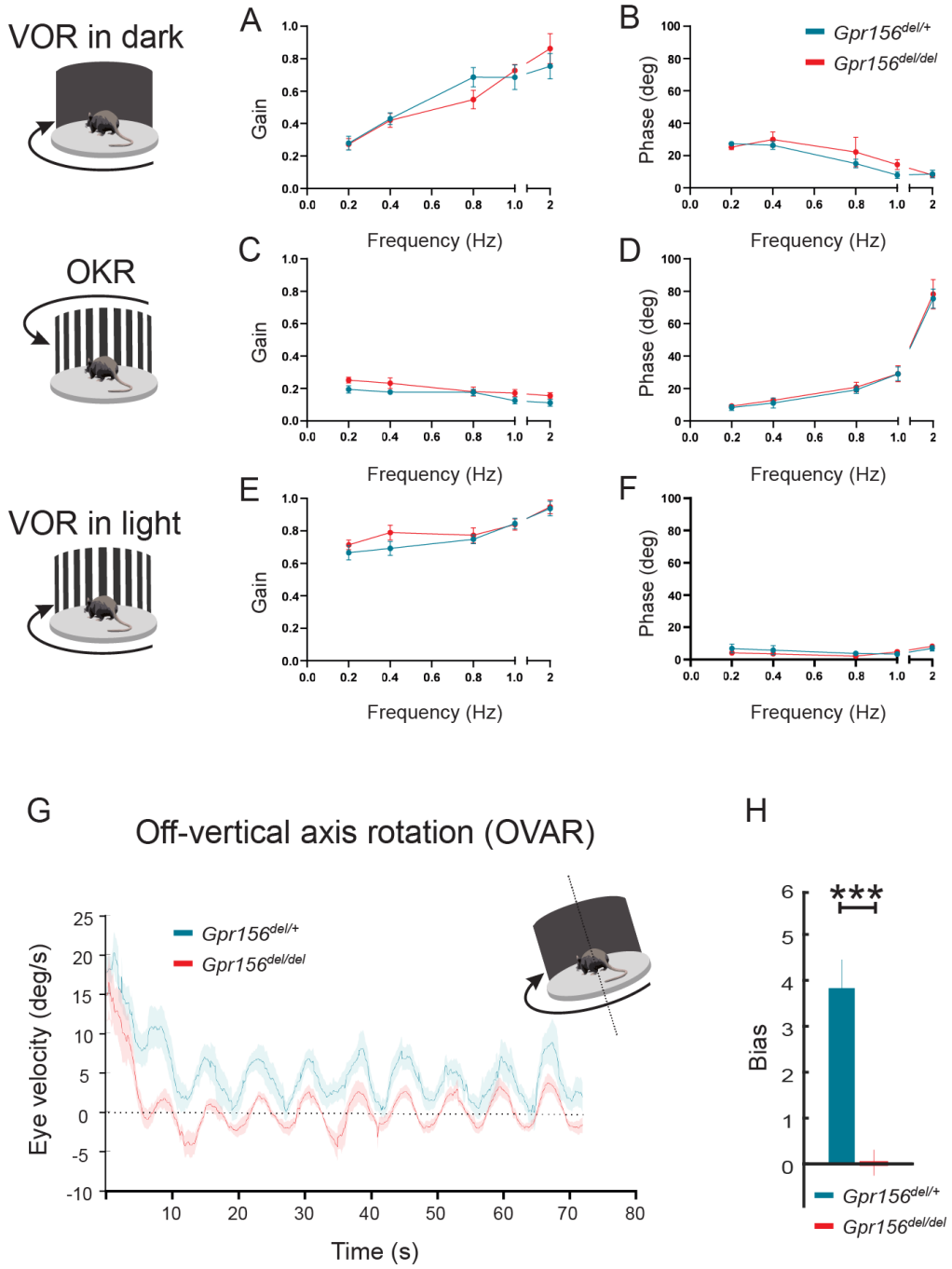

Figure 12. VOR and OKR responses were normal but OVAR responses were altered in *Gpr156*$^{del/del}$ mice. A-B) VORd gain and phase (mean±SEM) plotted as a function of frequency for control and *Gpr156*$^{del/del}$ mice. N is 8 and 7 for control (green) and *Gpr156*$^{del/del}$ KO (red) mice respectively. **C-D**) OKR gain and phase (mean±SEM) plotted as a function of frequency for control and *Gpr156*$^{del/del}$ mice. **E-F)** VORl gain and

1546 phase (mean±SEM) plotted as a function of frequency for control and *Gpr156*$^{del/del}$ mice.
1547 (**G**) Average eye velocities (mean±SEM) during 72s-long off-vertical axis rotation for
1548 control and *Gpr156*$^{del/del}$ mice. N is 8 and 7 for control (green) and *Gpr156*$^{-/-}$ (red) mice
1549 respectively. **H)** OVAR bias during the steady state (mean±SEM) for control and
1550 *Gpr156*$^{del/del}$ mice. ***P<0.001.
1551
1552
1553
1554
1555
1556
1557
1558
1559
1560
1561
1562
1563
1564

1565 **TABLES**

1566

1567

1568

1569 **Table 1. Percent of LES HCs with transduction**

1570

	Type I	Type II	ALL
Gpr156 $^{del/+}$	16/22 (73%)	23/38 (60%)	39/60 (65%)
Gpr156 $^{del/del}$	20/29 (69%)	34/46 (73%)	54/75 (72%)
Age range (median)	P11-44 (P19)	P11-100 (P19)	P11-P100 (P18)
p value	0.99	0.63	0.89

1571

1572

1573

1574 **Table 2. Genotype comparisons of transduction and adaptation in LES HCs**

			G(X) Boltzmann parameters				*Adaptation component tau at X-1/2*			*Adaptation component extent at at X-1/2*			
Genotype	**n**	**Age (median)**	G_{max}, nS	10-90%, nm	$X_{1/2}$, nm	dx, nm	τ_{VF}, ms (n)	τ_F, ms	τ_S, ms	% decay	% A_{VF}	% A_F	% A_S
Gpr156 $^{del/+}$	23	P8-32 (P18)	3.0 ± 0.2	0.66 ± 0.04	0.20 ± 0.01	0.16 ± 0.01	0.3 ± 0.1 (14) n.d. (9)	10.5 ± 1.8	152 ± 31	64 ± 2	24 ± 5 (14) n.d. (9)	39 ± 4	37 ± 3
Gpr156 $^{del/del}$	26	P8-32 (P20)	2.9 ± 0.2	0.72 ± 0.04	0.25 ± 0.02	0.16 ± 0.01	0.3 ± 0.3 (14) n.d. (12)	7.8 ± 1.0	140 ± 21	68 ± 3	24 ± 5 (14) n.d (12)	36 ± 4	40 ± 4
Statistics													
p value			0.91	0.26	0.11	0.9	0.44	0.18	0.75	0.3	0.95	0.67	0.62
NS power			0.05	0.2	0.36	0.05	0.12	0.27	0.06	0.18	0.05	0.07	0.08

Includes both cell types and all zones
*n.d. = very fast component not detected

1575

1576

1577 **Table 3. Genotype comparisons of electrical properties of Type I and II HCs in**
1578 **LES**
1579

HC type	Genotype	n	Age (median)	C_m, pF	V_{rest}, mV	$V_{1/2}$, mV	Slope factor, mV	R_{in} (MΩ)	G_{max}/C_m, nS/pF
Type I	*Gpr156*$^{del/+}$	9-13	P15-34 (P19)	5.8 ± 0.2	-85 ± 1	-83 ± 1	4.5 ± 0.3	46 ± 3	19 ± 2
	Gpr156$^{del/del}$	11-18	P12-44 (P18)	5.8 ± 0.3	-86 ± 1	-84 ± 1	4.8 ± 0.3	51 ± 3	24 ± 4
	p value			0.84	0.84	0.57	0.53	0.37	0.22
	*NS power			0.05	0.05	0.08	0.09	0.14	0.2
Type II	*Gpr156*$^{del/+}$	24-29	P11-47 (P18)	4.7 ± 0.1	-72 ± 1	-31 ± 1	8.9 ± 0.5	598 ± 35	2.7 ± 0.2
	Gpr156$^{del/del}$	28-29	P12-44 (P17)	4.4 ± 0.1	-73 ± 2	-30 ± 1	9.0 ± 0.6	575 ± 41	3.2 ± 0.2
	p value			0.14	0.71	0.48	0.85	0.67	0.11
	*NS power			0.31	0.07	0.1	0.05	0.07	0.34

1580
1581 *estimated power of non-significant result
1582
1583 **Table 4. Genotype comparison of G(X) and adaptation parameters for all hair cells**

			G(X) Boltzmann parameters				*Adaptation component tau at X-1/2*			*Adaptation component extent at at X-1/2*			
Genotype	**n**	**Age (median)**	G_{max}, nS	10-90%, nm	$X_{1/2}$, nm	dx, nm	τ_{VF}, ms (n)	τ_F, ms	τ_S, ms	% decay	% A_{VF}	% A_F	% A_S
Gpr156 $^{del/+}$	23	P8-32 (P18)	3.0 ± 0.2	0.66 ± 0.04	0.20 ± 0.01	0.16 ± 0.01	0.3 ± 0.1 (14) n.d. (9)	10.5 ± 1.8	152 ± 31	64 ± 2	24 ± 5 (14) n.d. (9)	39 ± 4	37 ± 3
Gpr156 $^{del/del}$	26	P8-32 (P20)	2.9 ± 0.2	0.72 ± 0.04	0.25 ± 0.02	0.16 ± 0.01	0.3 ± 0.3 (14) n.d. (12)	7.8 ± 1.0	140 ± 21	68 ± 3	24 ± 5 (14) n.d (12)	36 ± 4	40 ± 4
Statistics													
p value			0.91	0.26	0.11	0.9	0.44	0.18	0.75	0.3	0.95	0.67	0.62
NS power			0.05	0.2	0.36	0.05	0.12	0.27	0.06	0.18	0.05	0.07	0.08

Includes both cell types and all zones
*n.d. = very fast component not detected

1584
1585
1586

1587 **Table 5. Genotype comparison of excitability in LES afferents**

1588

Genotype	n	Age range (median)	# Transient	# Sustained	Vrest, mV	Rin, MΩ	I-threshold, pA
Gpr156$^{del/+}$	18	P11-35 (P19)	1 (5%)	17 (94.5%)	-66 ± 1	614 ± 145	111 ± 27
Gpr156$^{del/del}$	20	P13-35 (P16)	1 (5.0%)	19 (95.0%)	-67 ± 1	323 ± 67	105 ± 20
Statistics							
p value				0.99	0.20	0.09	0.85
***NS power**					0.25	0.43	0.05

1589

1590 *estimated power of non-significant result

1591

1592 **Supplemental Figures**

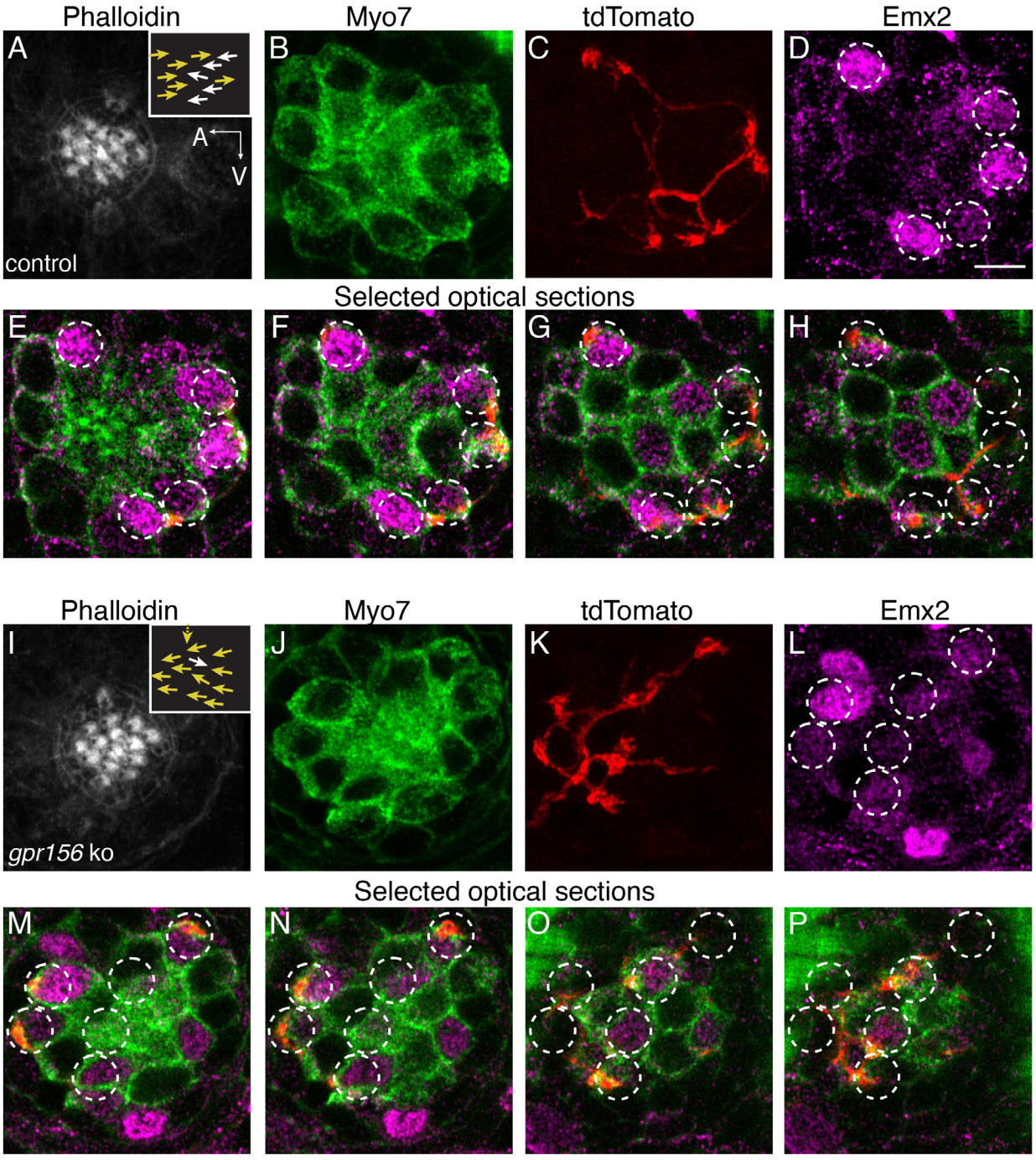

1593

1594

1595 **Supplemental figure 1. Gpr156 was not required for lateral-line afferents to select**
1596 **Emx2⁺ HCs. A-H)** Images of a control neuromast innervated by a single afferent fiber that
1597 contacts Emx2⁺ cells. (A) Phalloidin label reveals 14 hair bundles (7 A>P and 7 P>A hair
1598 bundles). Z-stack projections show all HCs labeled with Myo7a (**B**) a single afferent fiber
1599 expressing tdTomato (**C**) and Emx2⁺ and Emx2⁻ HCs (**D**). (**E-H**) Selected optical sections

1600 of (**B**–**D**) highlight the single afferent contacting individual Emx2$^+$ HCs. (**I**-**P**) Images of a
1601 *gpr156* mutant neuromast innervated by a single afferent fiber that contacts Emx2$^+$ cells.
1602 **I**) Phalloidin label revealed 14 hair bundles (12 A>P and 1 P>A hair bundles, 1 at 90°). Z-
1603 stack projections show all HCs labeled with Myo7a (**J**) a single afferent fiber expressing
1604 tdTomato (**K**) and Emx2$^+$ and Emx2$^-$ HCs (**L**). **M**-**O**) Selected optical sections of (**J**–**L**)
1605 highlight a single afferent in a *gpr156* mutants contacting individual Emx2$^+$ HCs. Arrows
1606 in **A** and **I** indicate the orientation of the hair bundles in each example. Scale bar: 5 μm.
1607

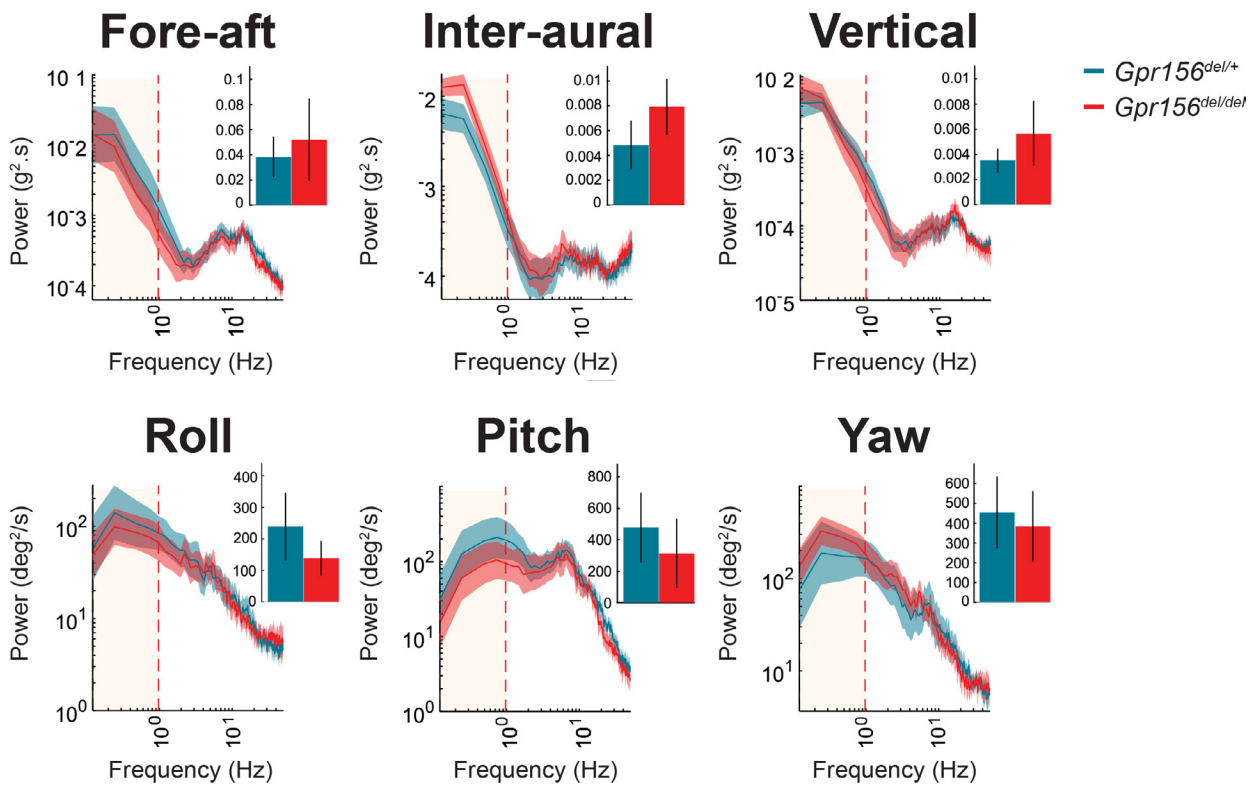

1608

1609 **Supplemental figure 2. No resting head tremor was observed in *Gpr156*$^{del/del}$ mice.**
1610 Comparison of power spectra density of head movements at rest in translational axes
1611 and rotational axes between control and *Gpr156*$^{del/del}$. N is 8 and 7 for control and
1612 *Gpr156*$^{del/del}$ mice respectively. Error bars: SEM.

1613

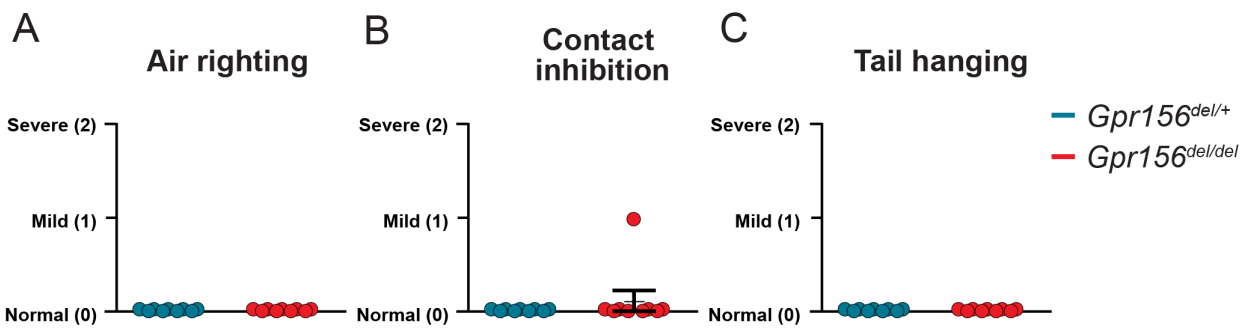

Supplemental figure 3. *Gpr156*$^{del/del}$ mice scored normally on several basic standard behavioral tests. Comparison of assigned scores between *Gpr156*$^{del/del}$ and control mice show no impairment in (**A**) air righting, (**B**) contact inhibition, (**C**) tail hanging. N is 9 and 7 for control and *Gpr156*$^{del/del}$ mice respectively. Error bars: SEM.

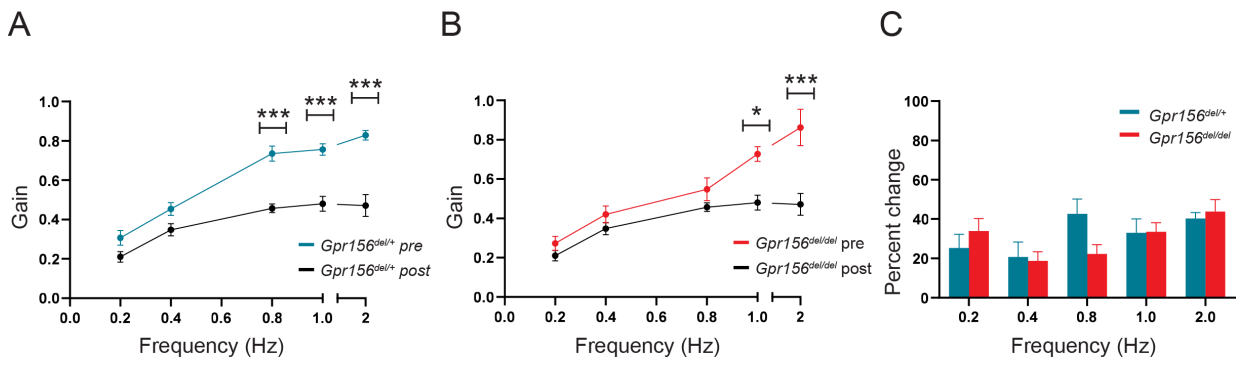

Supplemental figure 4. VOR learning was unimpaired in *Gpr156*$^{del/del}$ mice. A) VORd gain (mean ± SEM) before and after the VOR gain-down training plotted as a function of frequency for control mice (N=7). **B**) VORd gain (mean ± SEM) before and after the VOR gain-down training plotted as a function of frequency for *Gpr156*$^{del/del}$ mice (N=7). **C**) Percent change in VOR gain for control and *Gpr156*$^{del/del}$. *P<0.05, ***P<0.001.